OUKA
The University of Osaka
Institutional Knowledge Archive

Title	Research on Laser Plasma Acceleration by Particle-in-cell Simulation
Author(s)	周, 維民
Citation	大阪大学, 2009, 博士論文
Version Type	VoR
URL	https://hdl.handle.net/11094/134
rights	
Note	

The University of Osaka Institutional Knowledge Archive : OUKA

https://ir.library.osaka-u.ac.jp/

The University of Osaka

Research on Laser Plasma Acceleration by Particle-in-cell Simulation

January 2009

Weimin Zhou

Abstract

With the development of chirped-pulse-amplification (CPA), ultrahigh-intensity laser pulses now can easily exceed 10^{18} W/cm^2. Such high laser intensities have opened a new regime of high field science, including laser plasma accelerators because of the huge electric fields generated in intense laser plasma interactions. Such laser plasma accelerators are capable of producing beams of energetic electrons, protons and γ-rays.

Submitted to the Division of Electrical, Electronic and Information Engineering, Graduate School of Engineering, Osaka University in partial fulfillment of the requirements for the degree of Doctor of Philosophy, this thesis presents the research on laser plasma acceleration and relevant topics by particle-in-cell (PIC) simulation and theoretical analysis. The organization of this thesis is as follows.

In Chapter 1, from the advent of laser fusion concept to the current status of laser plasma acceleration, background of this thesis is introduced. Then the objective and outline of this thesis are presented.

In Chapter 2, starting from the principle and some special algorithms of PIC method, the development of PIC program of laser plasma interaction is discussed. For the research presented in this thesis, one-, two- and three-dimensional fully relativistic electromagnetic PIC programs are developed taking account of the spatial effects of the problems in which we are interested and the expenses of computer time. All PIC codes are programmed in Fortran language, and parallelized with Message Passing Interface (MPI) method.

In Chapter 3, a diagnostic method of measuring nonlinear evolution of laser wakefield by multiple sidebands of Raman scattering of a probe laser light is proposed. An analytical solution for the amplitudes of the sidebands is presented. To demonstrate the validation of the analytical solution, propagation of the probe pulse in wakefields is simulated with 1D PIC code. It is found that the analytical solution and the results of PIC simulations are well consistent with each other and other experiments. And the influence of plasma density, pump laser intensity, propagating length and nonlinearity of wakefield on the probe laser light has also been investigated by 1D PIC simulations. It is shown that this diagnostic method can be employed to measure the laser wakefield conveniently and widely.

In Chapter 4, acceleration of hot electron in intense laser cone plasma

interactions is studied via 2D PIC simulation. A new mechanism responsible for the generation of electron bunches along the plasma surface by obliquely incident laser is proposed. Re-acceleration effect of surface electron bunches at the cone tip is investigated by PIC simulations. It is demonstrated that the cone target can effectively guide hot electrons and laser energy to the cone tip, which results in higher coupling from laser to electrons. The confinement of hot electrons by double-wall cone target is simulated. Such double-wall cone target can confine hot electrons much better than single-wall cone target to the fuel capsule in fast ignition.

Chapter 5 studies one of wonderful applications of hot electrons in laser cone plasma interactions – proton beam acceleration. To increase the energy of accelerated proton beams, a scheme using cone-shaped target with a coated proton layer is presented and investigated via 2D PIC simulation. The results of 2D PIC simulation show that due to the guiding of laser and electrons along the cone wall, energy of hot electrons is enhanced by the cone target. Then the amplitude of sheath field on the target rear surface is enhanced since it is proportional to the temperature of hot electrons and logarithm of density, and so are the energies of proton beams which are accelerated by the sheath field. The key for the generation of monoenergetic protons is proved by simulation results. It is concluded that 200 MeV monoenergetic proton beams may be achieved with the currently available PW laser facility.

In Chapter 6, a new method of increasing laser intensity – focusing of intense laser via parabolic plasma concave surface is proposed. 3D PIC simulation is used to investigate the focusing conditions. The cases with various focal lengths and laser polarizations are compared. It is shown that the geometric focusing can increase the laser intensity by 2 orders of amplitude. If high harmonics produced from the reflection of incident laser and concave plasma surface are taken into account, the focused laser intensity can be increased further due to the smaller focal spot and compressed laser period to attoseconds.

In Chapter 7, the major conclusions of above researches are summarized.

Contents

Chapter 1 Introduction

1.1 Laser fusion

Controlled fusion reaction, which has been proposed to produce energy abundantly, cheaply, cleanly and safely, may be the long term solution to the global energy crisis of human being. Nuclear fusion can only occur at the extreme temperatures like in the center of a star where the velocities of thermal motion of the nuclei are sufficient to overcome the Coulomb repulsion. For controlled fusion, there are two possible approaches. One is magnetic confinement fusion (MCF) which confines the fusion fuel at moderate pressure by means of magnetic filed. The other possible approach is inertial confinement fusion (ICF), in which the fusion reaction is initiated by heating and compressing the fuel pellet of Deuterium and Tritium (D-T) with high energy beams of laser, electrons or ions. These high energy beams are called the driver.

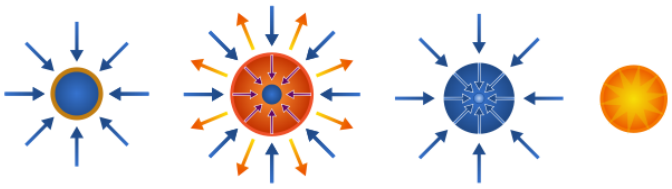

Fig. 1.1 Steps of laser fusion based on central ignition model

After invented in 1960, the laser was immediately recognized as an appropriate driver for ICF. The first open publication for laser fusion which appeared in 1972 [1] presented the central ignition model. Based on the central ignition model, the process for laser fusion consists of four steps: heat, compression, ignition and burn. First, laser beams rapidly heat the surface of tiny D-T fuel pellet to the temperature of several keV. Second, fuel is compressed to a density of ~400 g/cm^3 by the rocket-like blowoff of the hot surface plasma. Third, during the final part of the capsule implosion, the fuel core reaches the extreme conditions for nuclear fusion reaction. Finally, thermonuclear burn spreads rapidly through the compressed fuel, yielding many times of the input energy.

The calculation for laser fusion of central ignition with the understanding of the Rayleigh-Taylor instability and laser plasma instabilities implies to achieve the ignition the laser energy greater than 1 MJ is required. The laser intensities in the

range of 10^{14}-10^{15} W/cm^2 are appropriate for the laser fusion. In addition, the laser periods of several nanoseconds are necessary. For these reasons, Neodymium-Glass laser with wavelength of 1.06 μm is a good choice as the driver of laser fusion. Since shorter laser wavelengths have advantages of penetrating to higher densities of fuel pellet, some laser facilities work with frequency-doubled at 0.53 μm, or tripled at 0.35 μm.

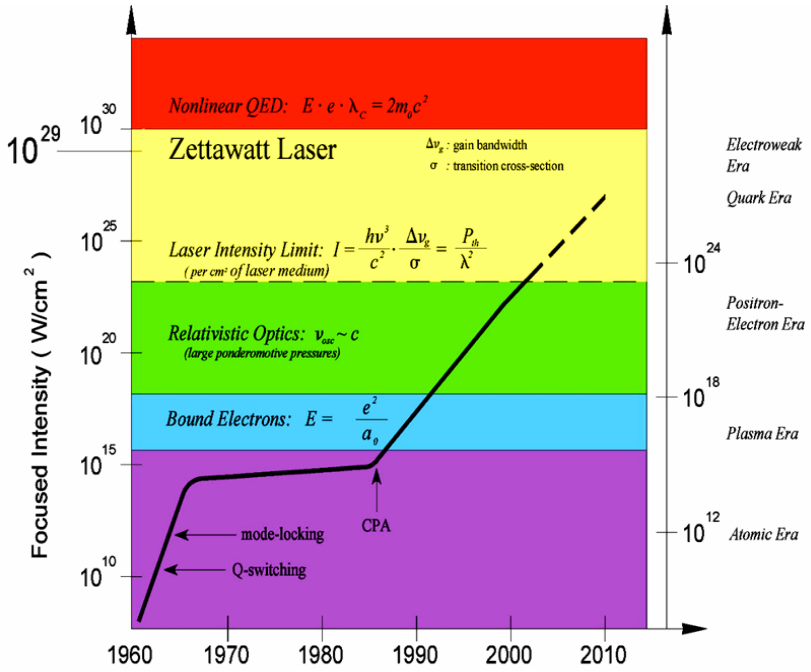

Fig. 1.2 Progress in peak laser intensity

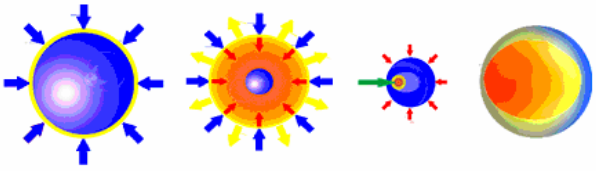

Fig. 1.3 Steps of laser fusion based on fast ignition model

With the development of chirped-pulse-amplification (CPA) technology [2], ultrahigh intensity laser pulses now can easily exceed 10^{18} W/cm^2. Such high laser intensities have opened a new regime of high field science, including fast ignition [3]. Fast ignition model consists of three phases as shown in Fig. 1.3. First, a capsule is imploded as in the conventional approach to ICF to assemble a high density fuel configuration. Second, a hole is bored through the capsule corona composed of ablated material, as the critical density is pushed close to the high density core of the

capsule by the ponderomotive force associated with high intensity laser light. Finally, the capsule is ignited by the superthermal electrons, produced in the high intensity laser plasma interactions, which then propagate from critical density to this high density core. Compared to the central ignition model, this fast ignition scheme drastically reduced the difficulty of implosion, and thereby allows lower quality target fabrication and less stringent beam quality and symmetry requirements from the implosion driver. The difficulty of the fusion scheme is transferred to the technical difficulty of producing the ultrahigh intensity laser and of transferring this energy to the fuel.

An alternative approach of fast ignition by inserting a hollow gold cone inside the spherical fuel capsule [4] has been proposed to avoid the propagation losses and deflection of the ultrahigh ignition laser pulses, and the transport of the relativistic electron beams through the high density plasma surrounding the fuel. A significant enhancement of the yield of neutron has been observed with this scheme [5]. A concept for fast ignition using proton beams was presented in Ref. [6]. This concept was motivated by the advantages of proton beams which maintain almost straight trajectories while propagating in corona plasma and compressed fuel capsule, the high coupling efficiency due to energetic proton beams deposit most of their energy in a small volume at the end of their range (Bragg peak), and the observation of intense high energy proton beams in petawatt laser solid interactions.

1.2 Laser plasma accelerator

The table-top sized laser plasma accelerator is another new field of high intensity laser plasma interaction. Laser plasma accelerators were proposed as a next generation compact accelerator because of the huge electric fields they can sustain. The accelerating electric fields in conventional accelerators are limited to a few tens of MeV/m, owing to material breakdown at the walls. Laser plasma accelerators can produce accelerating fields of hundreds of GeV/m, which accelerate particles to high energies in distances much shorter than in conventional accelerators. Such laser plasma accelerators are capable of producing beams of energetic electrons, protons and γ-rays.

One major laser plasma accelerator is laser wakefield accelerator (LWFA) [7]. While an intense short laser pulse is injected in tenuous plasmas, the ponderomotive force of laser light expels electrons both longitudinally and transversely from the high

intensity region. Then, a wave of strong electrostatic fields called wakefield is generated behind the pump laser. This is the so-called LWFA. If electrons with sufficient energy matching the accelerating electric fields are injected into the wakefield, they can be trapped by the wakefield and accelerated to high energy.

In the last fifteen years, several major injection schemes have been proposed and performed by experiments successfully. Self-injection resulting from wave breaking was a possible path to accelerate electrons to high energies [8]. The characteristics of the injected electrons by wave breaking of plasma wakefield wave were investigated in detail with PIC simulations [9]. Then V. Malka *et al*. carried out this scheme in experiment where 30 fs 3.0×10^{18} W/cm^2 laser pulses interacted with plasma with densities 2×10^{19} - 6×10^{19} cm^{-3}. The effective electron temperature was 18 MeV with maximum energy about 200 MeV. Another injection scheme where plasma density is sufficiently high (n_e~1.0×10^{19} cm^{-3}, E_0~300GV/m) that the laser pulse extend over many plasma wavelength was proposed and termed as the self-modulated LWFA (SMLWFA) by researchers in Naval Research Laboratory [10, 11]. Soon after, experiments based on this SMLWFA concept were carried out [12, 13] and obtained high-energy electron beams with maximum energy around 20 MeV.

In 2004, three experiments on the generation of monoenergetic electrons around 100 MeV were presented in Nature [14-16]. The possible mechanism accounting for the generation of monoenergetic electrons was the beam loading in bubble region [17]. The beam loading mechanism is a kind of self-injection of electrons into laser wakefield and depends strongly on the nonlinearity of pump laser propagation in plasma. In 2006, J. Faure *et al*. used a pump laser pulse at 3.4×10^{18} W/cm^2 and a injection laser pulse at 4×10^{17} W/cm^2 colliding in underdense plasma of 7.5×10^{18} cm^{-3} and obtained monoenergetic electron beams with energy of 117±7 MeV [18]. This injection scheme using two colliding laser beams was first proposed by D. Umstadter *et al*. [19], and then further developed by E. Esarey *et al*. [20]. Compared to the beam loading scheme in bubble region, this colliding scheme is stable so that the same monoenergetic electrons are produced in almost every shot of the experiments.

The other laser plasma accelerator is laser solid plasma accelerator. In the interactions of high intensity laser pulse with overdense plasma, high energy electrons are majorly produced by a variety of collisionless mechanisms such as resonance absorption [21], vacuum heating [22], and relativistic **J**×**B** heating [23]. These high energy electrons are called hot or fast or super-thermal electrons which have energies

much higher than the bulk plasma temperature. Thus, typical energy spectrum of electrons resulting from collisionless mechanisms has a bi-Maxwellian distribution where $T_h >> T_e$.

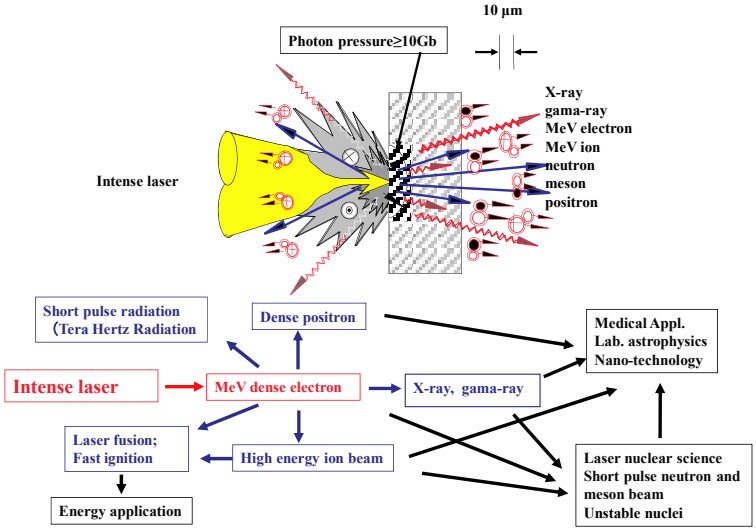

Fig. 1.4 Schemes of laser solid plasma accelerators

These collisionless mechanisms compete with each other and produce hot electrons with different energies. Based on the model of resonant absorption and assumption of quasiequilibrium state [24], the temperature of hot electrons was given as $T_h = 14(I\lambda^2)^{1/3} T_e^{1/3}$ keV , where I is the laser intensity in units of 10^{16} W/cm^2, λ is the laser wavelength in μm, and T_e is the temperature of background electrons in keV. This scaling law illustrates the temperature of hot electrons weakly scales with laser wavelength and laser intensity. As for the vacuum heating mechanism where intense laser pulse obliquely interacts with sharp gradient of overdense plasma, hot electron temperature is given as $T_h = 7(I\lambda^2)^{1/3}$ [25], which is similar to the scaling law in Ref. [24]. Another temperature scaling law of hot electrons based on relativistic **J**×**B** heating mechanism which is appropriate for normal incidence and laser intensities over 10^{18} W/cm^2 gave $T_h = 511[(1+0.73I\lambda^2)^{1/2} - 1]$ keV [26], where I is the laser intensity in 10^{18} W/cm^2.

Almost all applications of laser plasma accelerators depend critically on the generation of these high energy hot electrons, see Fig. 1.4. For example, the transfer of energy from the laser pulse to hot electrons is one of the critical issues for fast ignition. Furthermore, production of energetic ion beams in laser solid plasma interactions is directly related to the generation of hot electrons. With current CPA technology ions are not easy to be accelerated to high energy directly by the laser field

because of their much higher mass compared to that of electrons. However, in plasmas, intense laser lights interact with electrons and push them around; the electric fields via charge separation between electrons and ions are so high that the ions can be accelerated to high energies. From simple charge separation model, electric fields are induced by hot electrons rather than thermal ones. Thus, the mean ion energy is directly related to the potential generated by the hot electrons as $U_{ion} \propto k_B T_h$, here T_h is the temperature of hot electrons.

The emission of energetic ions in laser-plasma interactions for nanosecond time scale was first observed in experiment in 1960's [27, 28]. S. J. Gitmoer *et al*. analyzed the data on the production of energetic ions for a wide variety of laser wavelengths, energies as well as pulse lengths and presented five theoretical models to explain the correlation [28]. They found the predominant component of these energetic ions was protons accelerated both forward and backward to the laser incidence due to the blow-off expansion of bulk target plasma. These protons originate from the water vapor in the chamber or contaminant layer on the target surface. And a scaling law between the temperature of hot electrons and mean proton energies was confirmed based on the given theoretical models.

In the last fifteen years, a number of experiments on the generation of forward multi-MeV protons for CPA laser lights at intensities over 10^{18} W/cm^2 were reported and interpreted with remarkably different mechanisms for origin and acceleration. E. L. Clark *et al*. obtained 10^{12} protons with energies up to 18 MeV by irradiating a laser light of 1 ps at intensities of 5.0×10^{19} W/cm^2 onto a 125 μm aluminum target with incident angle of 45° [29]. The ions signal on the detectors exhibits a ring structure. They interpreted these ring-structured high-energy ions were shock-accelerated forward at the front surface of the target and deflected by ~30 MG magnetic fields produced by hot electrons leading the ions while propagating through the target. A similar explanation of frontside acceleration was presented by A. Maksimchuk *et al*. [30]. However, R. A. Snavely *et al*. argued that forward high-energy proton beams were accelerated by the laser ponderomotive force at the rear surface of the target, which was supported by the evidence that protons were emitted perpendicular to the rear surface of the target even for wedge-shaped targets [31]. In their experiment, PW laser pulses of 500 fs duration with peak intensity at 3.0×10^{20} W/cm^2 were focused onto different targets. Up to 48 J of the laser energy was transferred to 3.0×10^{18} protons > 10 MeV.

Although the mechanism accounting for the generation of these proton beams is not clear, experimental results showed that they are always normal to the back surface of the target, have a small angular aperture at the highest energies. The duration of the proton beams and energy are relevant to the laser and target parameters. These properties of the proton beams make them of particular interest in view of possible applications, such as proton fast ignition [6], proton diagnostic probe [32], proton therapy [33], and so on.

Primary challenge for laser plasma accelerator is how to increase or control the energy of accelerated particles. Laser plasma accelerators are built up on the basis of laser plasma interactions which are complex and related to a huge amount of parameters of laser light and plasma, such as laser duration, energy, intensity, polarization, plasma density, geometry, temperature, *etc*. This list is endless. It is impossible to study the influence of these parameters to the energy of accelerated particles one by one in experiments. On the other hand, some of these parameters are more important than the others. By changing the critical parameters, we can easily increase or control the energy of accelerated particles. Hence, physics of interaction should be understood clearly to determine which parameters are important and which are not so important for laser plasma accelerators. Diagnostics both in experiment and computer simulation can help understand the physics better.

1.3 Numerical simulation

Traditionally the behavior of complex physical systems has been investigated through theoretical approach and experimental approach. However, there are a large number of physical problems for which precise experiments and diagnostics are difficult or impossible, and the simultaneous nonlinear interaction of complex processes makes theoretical analysis difficult. For most of these problems, the fundamental laws that govern the system are clear, but we are simply unable to work out their consequences. With the advent of high speed computers, computer simulation based on the numerical physical model has been used for the numerical experiments which can give as much information about the details of the system as one desires.

Plasmas interacting with laser span a large range of densities and temperatures. According to the typical time and length scales of problems, numerical plasma models for effects we are interested in are generally classified into two categories: fluid or

kinetic. For fluid, or hydrodynamic model, the plasma state can be described by its macroscopic variables: density, pressure, fluid velocity *etc*. Based on the fluid equation of plasma and Maxwell's equations, hydrodynamic simulation is mainly used to investigate the large scale dynamic behavior of the plasma under the influence of electric and magnetic fields. Time scales of the hydrodynamic simulation are determined by the ion motion – typically from around a picosecond to several nanoseconds.

Kinetic simulation starting from Vlasov equation seeks to determine the distribution function $f(\mathbf{r}, \mathbf{v})$ of plasma self-consistently. Fokker-Plank simulation is such a kind of kinetic simulation looking for the particle distribution function. Particle-in-cell (PIC) method is another kind of kinetic simulation which is more economic than Fokker-Plank model. In PIC method, with the use of finite-size particle, as well as the spatial and temporal grids, the calculation is greatly reduced and the collisionless collective behavior of plasma can be simulated.

1.4 Objective and outline of this thesis

The major objective of this thesis is to help understand the physics of laser plasma acceleration via PIC simulation and theoretical analysis, and to explore new ways to increase energy and coupling from laser energy to the accelerated particles under current experimental conditions.

In Chapter 2, starting from the principle and some special algorithms of PIC method, the development of PIC program of laser plasma interaction is discussed.

In Chapter 3, a diagnostic method of measuring nonlinear evolution of laser wakefield by multiple sidebands of Raman scattering of a probe laser light is proposed. An analytical solution for the amplitudes of the sidebands is presented. To demonstrate the validation of the analytical solution, propagation of the probe pulse in wakefields is simulated with 1D PIC code. And the influence of plasma density, pump laser intensity, propagating length and nonlinearity of wakefield on the probe laser light has also been investigated by 1D PIC simulations.

In Chapter 4, acceleration of electrons in intense laser cone plasma interactions is studied via 2D PIC simulation. First, a new mechanism responsible for the generation of electron bunches along the plasma surface by obliquely incident laser is proposed. Second, re-acceleration effect of surface electron bunches at the cone tip is investigated by PIC simulations. Third, confinement of hot electrons by double-wall

cone target is simulated.

Chapter 5 studies one of wonderful applications of hot electrons in laser cone plasma interactions – proton beam acceleration. To increase the energy of accelerated proton beams, a scheme using cone-shaped target with a coated proton layer is presented and investigated via 2D PIC simulation. The key for the generation of monoenergetic protons is proved by simulation results.

In Chapter 6, a new method of increasing laser intensity – focusing of intense laser via parabolic plasma concave surface is proposed. 3D PIC simulation is used to investigate the focusing conditions. The cases with various focal lengths and laser polarizations are compared.

In Chapter 7, the major results of above researches are summarized.

Reference

1. Nuckolls, J., et al., *Laser Compression of Matter to Super-High Densities: Thermonuclear (CTR) Applications.* Nature, 1972. **239**(5368): p. 139-142.

2. Strickland, D. and G. Mourou, *Compression of amplified chirped optical pulses.* Optics Communications, 1985. **56**(3): p. 219-221.

3. Tabak, M., et al., *Ignition and high gain with ultrapowerful lasers.* Physics of Plasmas, 1994. **1**(5): p. 1626-1634.

4. Kodama, R., et al., *Fast heating of ultrahigh-density plasma as a step towards laser fusion ignition.* Nature, 2001. **412**(6849): p. 798-802.

5. Kodama, R., et al., *Nuclear fusion: Fast heating scalable to laser fusion ignition.* Nature, 2002. **418**(6901): p. 933-934.

6. Roth, M., et al., *Fast Ignition by Intense Laser-Accelerated Proton Beams.* Physical Review Letters, 2001. **86**(3): p. 436.

7. Tajima, T. and J.M. Dawson, *Laser Electron Accelerator.* Physical Review Letters, 1979. **43**(4): p. 267.

8. Dawson, J.M., *Nonlinear Electron Oscillations in a Cold Plasma.* Physical Review, 1959. **113**(2): p. 383.

9. Tzeng, K.C., W.B. Mori, and T. Katsouleas, *Electron Beam Characteristics from Laser-Driven Wave Breaking.* Physical Review Letters, 1997. **79**(26): p. 5258.

10. Sprangle, P., et al., *Propagation and guiding of intense laser pulses in plasmas.* Physical Review Letters, 1992. **69**(15): p. 2200.

11. Esarey, E., et al., *Trapping and Acceleration in Self-Modulated Laser Wakefields.* Physical Review Letters, 1998. **80**(25): p. 5552.

12. Modena, A., et al., *Electron acceleration from the breaking of relativistic plasma waves.* Nature, 1995. **377**(6550): p. 606-608.

13. Umstadter, D., et al., *Nonlinear Optics in Relativistic Plasmas and Laser Wake Field Acceleration of Electrons.* Science, 1996. **273**(5274): p. 472-475.

14. Mangles, S.P.D., et al., *Monoenergetic beams of relativistic electrons from intense laser-plasma interactions.* Nature, 2004. **431**(7008): p. 535-538.

15. Geddes, C.G.R., et al., *High-quality electron beams from a laser wakefield accelerator using plasma-channel guiding.* Nature, 2004. **431**(7008): p. 538-541.

16. Faure, J., et al., *A laser-plasma accelerator producing monoenergetic electron beams.* Nature, 2004. **431**(7008): p. 541-544.

17. Pukhov, A. and J. Meyer-ter-Vehn, *Laser wake field acceleration: the highly non-linear broken-wave regime.* Applied Physics B: Lasers and Optics, 2002. **74**(4): p. 355-361.

18. Faure, J., et al., *Controlled injection and acceleration of electrons in plasma wakefields by colliding laser pulses.* Nature, 2006. **444**(7120): p. 737-739.

19. Umstadter, D., J.K. Kim, and E. Dodd, *Laser Injection of Ultrashort Electron Pulses into Wakefield Plasma Waves.* Physical Review Letters, 1996. **76**(12): p. 2073.

20. Esarey, E., et al., *Electron Injection into Plasma Wakefields by Colliding Laser Pulses.* Physical Review Letters, 1997. **79**(14): p. 2682.

21. Ebrahim, N.A., et al., *Hot Electron Generation by the Two-Plasmon Decay Instability in the Laser-Plasma Interaction at 10.6 mum.* Physical Review Letters, 1980. **45**(14): p. 1179.

22. Brunel, F., *Not-so-resonant, resonant absorption.* Physical Review Letters, 1987. **59**(1): p. 52.

23. Kruer, W.L. and K. Estabrook, *J x B heating by very intense laser light.* Physics of Fluids, 1985. **28**(1): p. 430-432.

24. Forslund, D.W., J.M. Kindel, and K. Lee, *Theory of Hot-Electron Spectra at High Laser Intensity.* Physical Review Letters, 1977. **39**(5): p. 284.

25. Gibbon, P. and A.R. Bell, *Collisionless absorption in sharp-edged plasmas.* Physical Review Letters, 1992. **68**(10): p. 1535.

26. Wilks, S.C., et al., *Absorption of ultra-intense laser pulses.* Physical Review Letters, 1992. **69**(9): p. 1383.

27. Linlor, W.I., *Ion Energies Produced by Laser Giant Pulse.* Applied Physics Letters, 1963. **3**(11): p. 210-211.

28. Gitomer, S.J., et al., *Fast ions and hot electrons in the laser--plasma interaction.* Physics of Fluids, 1986. **29**(8): p. 2679-2688.

29. Clark, E.L., et al., *Measurements of Energetic Proton Transport through Magnetized Plasma from Intense Laser Interactions with Solids.* Physical Review Letters, 2000. **84**(4): p. 670.

30. Maksimchuk, A., et al., *Forward Ion Acceleration in Thin Films Driven by a High-Intensity Laser.* Physical Review Letters, 2000. **84**(18): p. 4108.

31. Snavely, R.A., et al., *Intense High-Energy Proton Beams from Petawatt-Laser Irradiation of Solids.* Physical Review Letters, 2000. **85**(14): p. 2945.

32. Borghesi, M., et al., *Macroscopic Evidence of Soliton Formation in Multiterawatt*

Laser-Plasma Interaction. Physical Review Letters, 2002. **88**(13): p. 135002.

33. Bulanov, S.V., et al., *Oncological hadrontherapy with laser ion accelerators.* Physics Letters A, 2002. **299**(2-3): p. 240-247.

Chapter 2 Particle-in-cell Simulation of Laser Plasma Interaction

2.1 Introduction

Particle-in-cell method [1-3] is simple and straightforward: numerically follow the motion of a large collection of charged particles in their self-consistent electric and magnetic fields. The basic cycle is illustrated in Fig. 2.1. From the positions and velocities of charged particles, the charge and current densities on the spatial grids are calculated. With these charge and current densities, the self-consistent electric and magnetic fields on the grids are computed next. Then electric and magnetic fields impact on the charged particles. Finally the positions and velocities of these charged particles are advanced. The basic cycle runs round by round to simulate the plasma problems we are interested in.

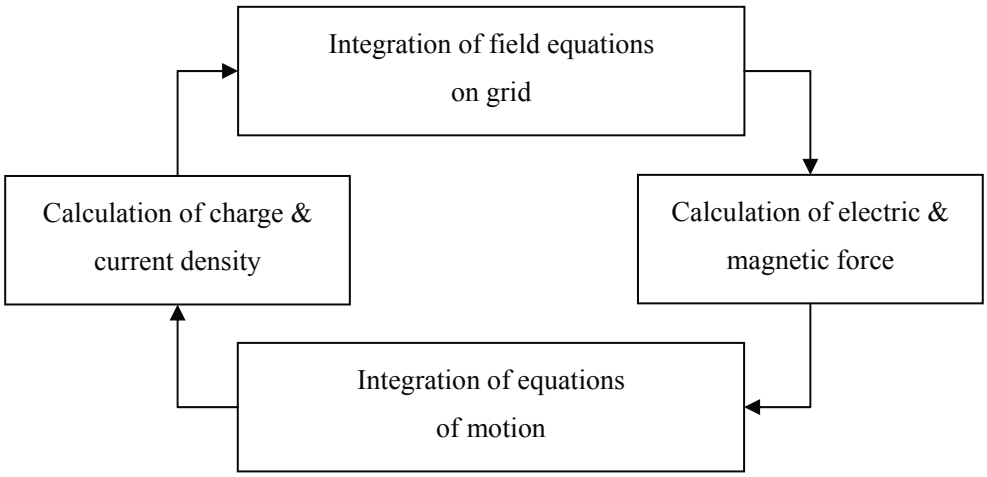

Fig. 2.1 The basic cycle of particle-in-cell simulation

If one attempts to solve the motions for a large number of real particles by directly computing the forces on them from Coulomb's law, he will soon realize that such an approach is impractical since the number of real particles is so huge that even the most powerful computer of today is not able to deal with such a huge calculation. Fortunately, what we are interested in is the collective behavior of plasma which occurs on a space scale greater than or comparable to the electron Debye length rather than the fine scale fluctuating microfield associated with discrete particle collisions.

In PIC simulation, we use finite-size particle which usually has the size comparable to the electron Debye length to represent many real particles, and divide the space into cells which have the spacing about equal to the size of the particle, see

Fig.2.2. With the use of finite-size particle and spatial grids, the calculation and rapidly varying force associated with close encounters are greatly reduced. However, the long-range Coulombic force which gives rise to collective motion is retained, and effects with scale greater than the size of cells (or particles) are accurately modeled.

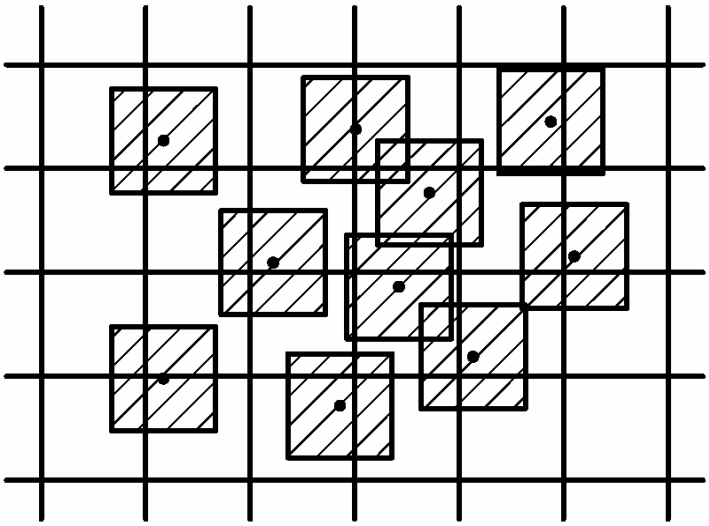

Fig. 2.2 Schematic of finite-size particles and cells in PIC model

For researches presented in this thesis, one-, two- and three-dimensional fully relativistic electromagnetic PIC programs are developed taking account of the spatial effects of the problems in which we are interested and the expenses of computer time. All PIC codes are programmed in Fortran language which has advantages in scientific calculations, and parallelized with Message Passing Interface (MPI) method for PC cluster at the Cybermedia Center in Osaka University.

2.2 Principle of PIC method

On the basis of two-dimensional relativistic electromagnetic model, we will introduce the principle and algorithms used in our PIC programs in detail. Most of these algorithms can be transferred to the one-dimensional and two-dimensional cases easily.

2.2.1 Integration of the field equations

From charge and current densities on the spatial grids as sources, we obtain the electric and magnetic fields by Maxwell's equations.

$$\nabla \cdot \mathbf{E} = \frac{\rho}{\varepsilon} \tag{2.1}$$

$$\nabla \times \mathbf{E} = -\frac{\partial \mathbf{B}}{\partial t} \tag{2.2}$$

$$\nabla \cdot \mathbf{B} = 0 \tag{2.3}$$

$$\nabla \times \mathbf{B} = \mu \mathbf{J} + \mu\varepsilon \frac{\partial \mathbf{E}}{\partial t} \tag{2.4}$$

In the 2D electromagnetic PIC model, the electric and magnetic fields are obtained from Faraday's law and Ampere-Maxwell law (Eqs. (2.2) and (2.4)). In accordance to the time derivatives of B and E fields, leap-frog scheme for the time integration is used (see Fig. 2.3). The leap-frog scheme is also appropriate for the time stepping of the charge and current densities, as well as the particle position and velocity.

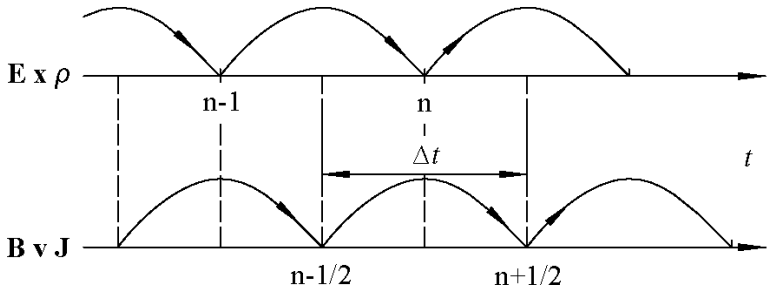

Fig. 2.3 Temporal layout of field and particle quantities used in leap-frog scheme

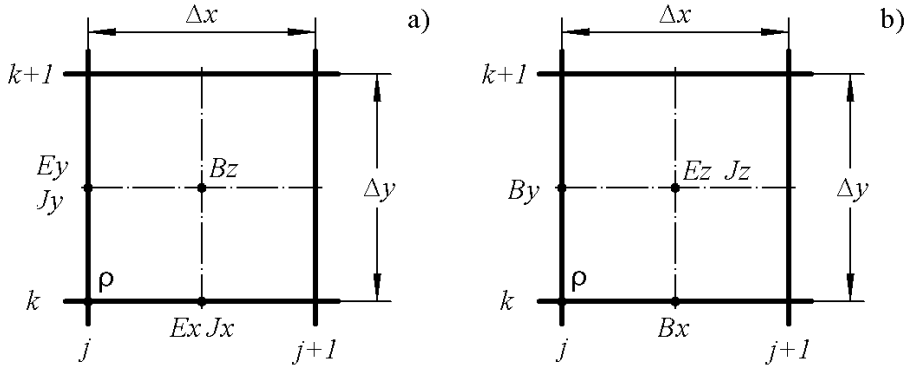

Fig. 2.4 Spatial layouts of a) TM and b) TE components, charge density on grid points

For 2D electromagnetic model, the fields are divided into transverse magnetic TM (sufficient for 2D simulation) and transverse electric TE (for $2_{1/2}$D and 3D simulations) sets. All spatial variation, and therefore **k** is in the *X*, *Y* plane. The TM fields, with $\mathbf{k}\cdot\mathbf{B}=0$, have components E_x, E_y and B_z. The TE fields, with $\mathbf{k}\cdot\mathbf{E}=0$, have components B_x, B_y and E_z. The relative spatial locations of components of these sets are shown in Fig. 2.4. The finite difference equations for TM components are

$$\frac{B^{n+1/2}_{z,j+1/2,k+1/2}-B^{n-1/2}_{z,j+1/2,k+1/2}}{\Delta t}=-\frac{E^{n}_{y,j,k+1/2}-E^{n}_{y,j+1,k+1/2}}{\Delta x}+\frac{E^{n}_{x,j+1/2,k+1}-E^{n}_{x,j+1/2,k}}{\Delta y} \tag{2.5}$$

$$\frac{E^{n+1}_{x,j+1/2,k}-E^{n}_{x,j+1/2,k}}{\Delta t}=\frac{B^{n+1/2}_{z,j+1/2,k+1/2}-B^{n+1/2}_{z,j+1/2,k-1/2}}{\mu\varepsilon\Delta y}-\frac{J^{n+1/2}_{x,j+1/2,k}}{\varepsilon} \tag{2.6}$$

$$\frac{E^{n+1}_{y,j,k+1/2}-E^{n}_{y,j,k+1/2}}{\Delta t}=\frac{B^{n+1/2}_{z,j+1/2,k+1/2}-B^{n+1/2}_{z,j+1/2,k-1/2}}{\mu\varepsilon\Delta x}-\frac{J^{n+1/2}_{y,j,k+1/2}}{\varepsilon} \tag{2.7}$$

When $B_z^{n-1/2}$ and En are known, $B_z^{n+1/2}$ is determined by Eq. (2.5). Then the electric field is advanced from Eqs. (2.6) and (2.7). TE components can be calculated in similar way.

2.2.2 Integration of the particle equations of motion

The particle equations of motion are

$$m\frac{d\mathbf{v}}{dt}=q(\mathbf{E}+\mathbf{v}\times\mathbf{B}) \tag{2.8}$$

$$\frac{d\mathbf{r}}{dt}=\mathbf{v} \tag{2.9}$$

where q and m are the charge and mass of particle. In relativistic case, we use $\mathbf{u}\equiv\gamma\mathbf{v}$ rather than **v**, where $\gamma=\sqrt{1-u^2}$ is the relativistic factor. The centered-difference form of the Newton-Lorentz equation is given by

$$\frac{\mathbf{u}^{n+1/2}-\mathbf{u}^{n-1/2}}{\Delta t}=\frac{q}{m}(\mathbf{E}^{n}+\frac{\mathbf{u}^{n+1/2}+\mathbf{u}^{n-1/2}}{2\gamma^{n}}\times\mathbf{B}^{n}) \tag{2.10}$$

We use the method of Boris to calculate $u^{n+1/2}$. Define u^+ and u^- as

$$\mathbf{u}^{n-1/2} = \mathbf{u}^{-} - \frac{q\mathbf{E}^{n}\Delta t}{2m} \tag{2.11}$$

$$\mathbf{u}^{n+1/2} = \mathbf{u}^{+} - \frac{q\mathbf{E}^{n}\Delta t}{2m} \tag{2.12}$$

Center γ and B by time averaging and substitute the above equations into Eq. (2.10) to obtain

$$\frac{\mathbf{u}^{+} - \mathbf{u}^{-}}{\Delta t} = \frac{q}{2m\gamma^{n}}(\mathbf{u}^{+} + \mathbf{u}^{-}) \times \mathbf{B}^{n} \tag{2.13}$$

Adding half of the electric impulse, $\mathbf{u}^{-}$ is obtained from Eq. (2.11). Using Boris' rotation, $\mathbf{u}^{+}$ can be calculated by

$$\mathbf{u}' = \mathbf{u}^{-} + \mathbf{u}^{-} \times \mathbf{t} \tag{2.14}$$

$$\mathbf{u}^{+} = \mathbf{u}^{-} + \mathbf{u}' \times \mathbf{s} \tag{2.15}$$

where $t=qB^{n}\Delta t/2me\gamma^{n}$, $s=2t/(1+t^{2})$. Finally adding the remaining half of the electric impulse from Eq. (2.12), $\mathbf{u}^{n+1/2}$ can be obtained. Then the position is advanced by

$$\mathbf{r}^{n+1} = \mathbf{r}^{n} + \mathbf{v}^{n+1/2}\Delta t = \mathbf{r}^{n} + \frac{\mathbf{u}^{n+1/2}\Delta t}{\gamma^{n+1/2}} \tag{2.16}$$

2.2.3 Particle weighting, charge and current densities

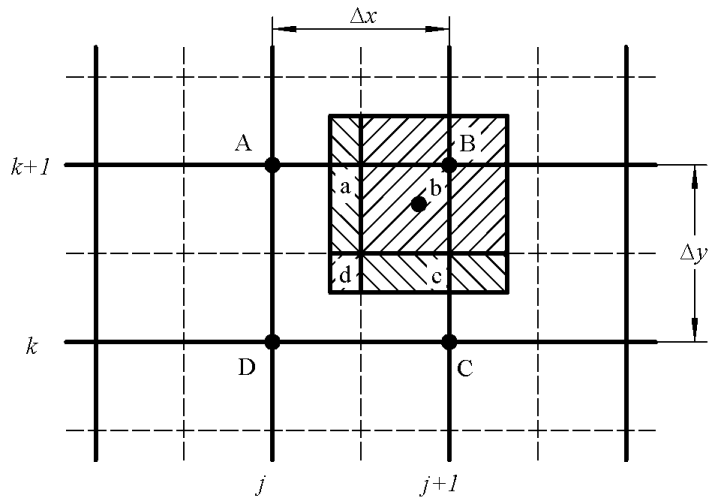

Fig. 2.5 Charge assignment for first order weighting in 2D

To obtain the fields on the discrete spatial grid points and forces on particles, it is necessary to calculate the charge and current densities on grid points and transfer the fields from the discrete grid points to the continuous particle positions. The processes are carried out through some form of interpolation between the grid points and particles, which is called weighting.

The charge density at position r_j contributed by a simulation particle whose center is at r is changed from $q\delta(r_j - r)$ for a point particle to $qS(r_j - r)$ for a finite-size particle, where $S(r_j - r)$ is a shape factor giving the way how a particle is contributing to the nearby spatial grid points and how the fields on these spatial grid points impulse the particle. In this way, the charge and current densities are given by

$$\rho(\mathbf{r}_j) = \sum_i q_i S(\mathbf{r}_j - \mathbf{r}_i) \tag{2.17}$$

$$\mathbf{j}(\mathbf{r}_j) = \sum_i q_i \mathbf{v}_i S(\mathbf{r}_j - \mathbf{r}_i) \tag{2.18}$$

where r_i, q_i and v_i are the central position and charge of *ith* particle. And the force on the particle is interpolated from the grid electric field with the same shape factor to avoid a self-force, as

$$\mathbf{F}_i = q_i \Delta\mathbf{r} \sum_j \mathbf{E}_j S(\mathbf{r}_j - \mathbf{r}_i) \tag{2.19}$$

The commonly used weightings include zero-order, first-order and high-order weightings. For all PIC codes for the research in this thesis, first-order weighting is employed. With two space dimensions, first-order weighting is called area interpolation as illustrated in Fig. 2.5. The ith particle has central position x_i, y_i, related to the grid point $X_j = j\Delta x$, $Y_k = k\Delta y$. The charge densities assigned to the nearest four grid points are proportional to the areas belonging to the grid points, that is

$$\rho_{j,k} = \rho_c \frac{[\Delta x - (x_i - X_j)][\Delta y - (y_i - Y_k)]}{\Delta x \Delta y} \tag{2.20}$$

$$\rho_{j+1,k} = \rho_c \frac{(x_i - X_j)[\Delta y - (y_i - Y_k)]}{\Delta x \Delta y} \tag{2.21}$$

$$\rho_{j,k+1} = \rho_c \frac{[\Delta x - (x_i - X_j)](y_i - Y_k)}{\Delta x \Delta y} \tag{2.22}$$

$$\rho_{j+1,k+1} = \rho_c \frac{(x_i - X_j)(y_i - Y_k)}{\Delta x \Delta y} \tag{2.23}$$

where ρ_c is the charge density uniformly filling a cell (q/area). In the same way, the fields of nearest four particles can be assigned back to the particle and impulse it.

2.2.4 Charge conservation algorithm

In Sec. 2.2.1, we mentioned that the fields are obtained from Faraday's law and Ampere-Maxwell law. However, there are two other Maxwell's equations. Firstly, if the divergences of E and B are correct initially,

$$\partial_t(\partial_x \cdot \mathbf{B}) = \partial_x \cdot (\partial_t \mathbf{B}) = -\partial_x \cdot \partial_x \times \mathbf{E} \equiv 0 \tag{2.24}$$

Eq. (2.3) is satisfied. Similarly, if J and ρ satisfy the continuity equation, Gauss' law remains satisfied, that is

$$\partial_t(\partial_x \cdot \mathbf{E} - \rho) = \partial_x \cdot \mathbf{J} - \partial_t \rho = 0 \tag{2.25}$$

If the current densities are derived from Eq. (2.18), the continuity equation for charge is not satisfied exactly. In this case, Poisson's equation is to be solved to correct the fields. However, to avoid solving Poisson's equation, there are several numerical techniques for solving the continuity equation locally [4-7]. They are called "charge conservation methods".

In the developed PIC programs in this thesis, the Zigzag scheme [7] based on the charge conversation method described by Eastwood [4] is used, where the current densities are

$$J^{n+1/2}_{x,j+1/2,k} = \frac{1}{\Delta x \Delta y} F_x (1 - W_y), \quad J^{n+1/2}_{x,j+1/2,k+1} = \frac{1}{\Delta x \Delta y} F_x W_y$$

$$J^{n+1/2}_{y,j,k+1/2} = \frac{1}{\Delta x \Delta y} F_y (1 - W_x), \quad J^{n+1/2}_{y,j+1,k+1/2} = \frac{1}{\Delta x \Delta y} F_y W_x \tag{2.26}$$

where F_x, F_y represents charge flux given by

$$F_x = q \frac{x^{n+1} - x^n}{\Delta t}, \quad F_y = q \frac{y^{n+1} - y^n}{\Delta t} \tag{2.27}$$

and W_x, W_y represents the first order shape factor defined at the midpoint between the

start point (x_n, y_n) and the end point (x_n +1, y_n +1)

$$W_x = \frac{x^{n+1} + x^n}{2\Delta x} - j\,,\quad W_y = \frac{y^{n+1} + y^n}{2\Delta x} - k \tag{2.28}$$

When the particle moves across cell meshes, four cases need to be considered depending on positions of the particle at time $n\Delta t$ and $(n + 1)\Delta$t. In the Zigzag scheme, a relay point of particle movement (x_r, y_r) is introduced to reduce the complexity of programming. The positions of the relay point are

$$x_r = \begin{cases} (x^n + x^{n+1})/2, & \text{for } j^n = j^{n+1} \\ \max(j^n \Delta x, j^{n+1}\Delta x), & \text{for } j^n \neq j^{n+1} \end{cases} \tag{2.29}$$

$$y_r = \begin{cases} (y^n + y^{n+1})/2, & \text{for } k^n = k^{n+1} \\ \max(k^n \Delta y, k^{n+1}\Delta y), & \text{for } k^n \neq k^{n+1} \end{cases} \tag{2.30}$$

In the PIC programs, the computation of the relay point is performed by

$$x_r = \min\{\min(j^n\Delta x, j^{n+1}\Delta x) + \Delta x, \max[\max(j^n\Delta x, j^{n+1}\Delta x), (x^n + x^{n+1})/2]\}$$

$$y_r = \min\{\min(k^n\Delta y, k^{n+1}\Delta y) + \Delta y, \max[\max(k^n\Delta y, k^{n+1}\Delta y), (y^n + y^{n+1})/2]\} \tag{2.31}$$

without any "IF" statement, which speeds up the computation.

2.2.5 Unit scale

In the laser-plasma interaction, some physical quantities are very tiny, like electron mass, charge, or laser wavelength, while other physical quantities are very huge, like light speed in vacuum or underdense plasmas. In order to avoid the error of computer calculating these significantly different quantities, appropriate units scaling should be used. In all PIC simulations in this thesis, variables are scaled with laser frequency or wavelength as follows

1) Coordinates are scaled to the laser wavelength λ_0: $x' = x/\lambda_0$;
2) Time is scaled to the laser period τ_0: $t' = t/\tau_0$;
3) Velocity is scaled to the light velocity in vacuum c: $v' = v/c$;
4) Simulation particle charge is scaled to the charge of single electron e: $q' = q/e$;
5) Simulation particle mass is scaled to the mass of electron m_e: $m' = m/m_e$;
6) Densities are given in units of the critical density $n_c = \omega_0^2\varepsilon_0 m_e/e^2$: $n' = n/n_c$;
7) Fields are scaled as $E' = eE/m_e\omega_0 c$, $B' = eB/m_e\omega_0$, where ω_0 is the laser frequency;

8) Energies are scaled to $m_e n_c c^2 \Delta x \Delta y \Delta z$ for 3D case; or $m_e n_c c^2 L \Delta x \Delta y$ for 2D case, where L is an arbitrary depth; or $m_e n_c c^2 A \Delta x \Delta y$ for 1D case, where A is an arbitrary cross section.

After the scaling of unit, the form of all equations is kept the same, only the factors are changed.

2.2.6 Diagnostics

Like most of other simulations, PIC simulation can supply as much information of the physics of plasma as we want. The output consists of data during the run (snapshots) and at the end (time histories) for fields and particles.

1) For particles:

The output data for particles include particle distributions in the phase space (vx versus x) and velocity space (v_x versus v_y), particle energy spectrum $f(v)$, trajectories of interested particles, total energy of different species, etc.

2) For fields:

The output data for fields include n-dimensional spatial distributions of electron density ($n_e(r)$), ion density ($n_i(r)$), temporal and averaged electric and magnetic fields ($E(r)$ and $B(r)$), laser energy density ($W(r)$), etc.

All data are outputted from the PIC codes and storied in ASCII format, and then are dealt with some data processing software.

2.3 Parallelization of PIC program

To keep the time integration of fields and particles accurate, Courant conditions should be satisfied as

$$(c\Delta t)^2 \left(\frac{1}{\Delta x^2} + \frac{1}{\Delta y^2} \right) < 1 \qquad (2.32)$$

that is $c\Delta t < \Delta x / \sqrt{2}$ for $\Delta x = \Delta y$ in 2D PIC scheme. The size of spacing of grid and particle is about of Debye length (λ_D) in order to simulate the collective behavior of plasma of space scale greater than or comparable to λ_D. Debye length $\lambda_D = (kBT_e/4\pi n_e e^2)^{1/2} \approx 0.018(n_c T_e/n_e)^{1/2}\lambda_0$, n_c is the critical density, T_e is the temperature in keV, n_e is the electron density, and λ_0 is the wavelength of incident laser light. For example, when λ_0 = 1.0 μm, T_e = 1.0 keV, and n_c/n_e = 1, Debye length λ_D= 0.018 μm. If Δx = 0.02 μm is used, typically $10^6/10^9$ grids and $10^7/10^{10}$ particles are needed to simulate the system with scale of tens of microns in 2D/3D PIC simulations. For such

a system, a huge amount of storage in memory is required. On the other hand, for interaction time of picosecond, about 10^5 steps of computation is required and costs tens to hundreds of hours of real computer time due to the current CPU ability.

The usage of parallel PIC algorithm [8] on supercomputers or PC clusters which distribute the computation among multiple processors made the simulation of large size and long time acceptable. There are two types of parallel PIC algorithms: first is to distribute particles into different processors. Second is to distribute both space and particles into different processors. For the latter type, as particles move from one region to another, they are moved to the processor which computes the corresponding region. The parallelization of it is higher than the former. But the passing of particles and interpolation of field data are more complex and need more performance of programming.

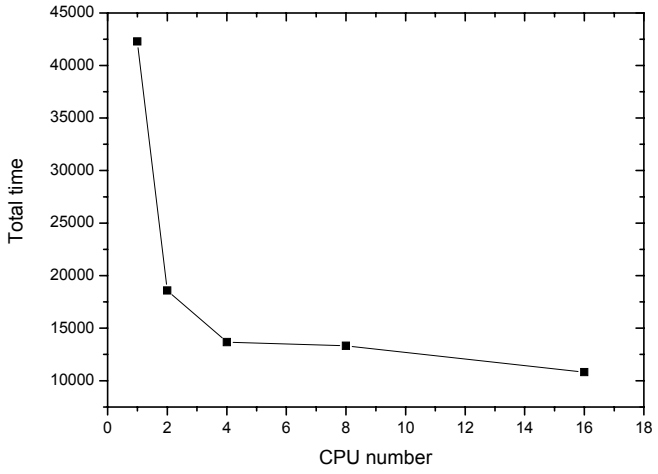

Fig. 2.6 Total time vs number of processor

The former parallel algorithm is exploited in PIC programs for researches in this thesis and carried out through message passing interface (MPI) library. The programs are in FORTRAN language and performed on PC cluster of the Cybermedia Center in Osaka University. Results of benchmark of 2D parallel PIC simulation with different processor number are shown in Fig. 2.6. We can see, when one processor was used, the calculation took about 42,000 seconds. When four processors were used, it took about 18,000 seconds, more than 2 times faster than one processor. But when the number of process is higher than four, there is no more obvious increase. Thus, four processors were used for the parallel PIC simulations presented in this thesis.

2.4 Conclusion

In this chapter, the model of PIC method is introduced to help understand why PIC code has ability simulating laser plasma interactions. For problems with different spatial effects, one-, two- and three-dimensional PIC programs were developed and exploited to research the laser plasma interaction in this thesis.

Reference

1. Dawson, J.M., *Particle simulation of plasmas.* Reviews of Modern Physics, 1983. **55**(2): p. 403.

2. Hockney, R.H. and J.W. Eastwood, *Computer simulation using particles*. 1988: McGraw-Hill.

3. Birdsall, C.K. and A.B. langdon, *Plasma physics via computer simulation*. 1991: McGraw-Hill.

4. Eastwood, J.W., *The virtual particle electromagnetic particle-mesh method.* Computer Physics Communications, 1991. **64**(2): p. 252-66.

5. Villasenor, J. and O. Buneman, *Rigorous charge conservation for local electromagnetic field solvers.* Computer Physics Communications, 1992. **69**(2-3): p. 306-316.

6. Esirkepov, T.Z., *Exact charge conservation scheme for Particle-in-Cell simulation with an arbitrary form-factor.* Computer Physics Communications, 2001. **135**(2): p. 144-153.

7. Umeda, T., et al., *A new charge conservation method in electromagnetic particle-in-cell simulations.* Computer Physics Communications, 2003. **156**(1): p. 73-85.

8. Liewer, P.C. and V.K. Decyk, *A general concurrent algorithm for plasma particle-in-cell simulation codes.* Journal of Computational Physics, 1989. **85**(2): p. 302-322.

Chapter 3 Diagnostic of Nonlinear Laser Wakefield by Raman Scattering of Probe Laser Light

3.1. Introduction

Since first suggested by Tajima and Dawson [1] about three decades ago, laser wakefield acceleration (LWFA) has been studied in theory [2-7], simulation [8-10], and experiment [11-13] because of its promising application as a compact laser plasma accelerator. Due to the large amplitude electric fields related to wakefields, electrons with sufficient energy that matches the phase of the accelerating fields can be trapped and accelerated to highly relativistic energy of the order of hundreds of MeV. For the electrons to be trapped and accelerated, they need to be injected into the wakefield with sufficient energy which matches the accelerating phase. Several injection schemes have been proposed [7, 9, 14-16] and demonstrated in experiments [11-13, 17-24] successfully. These injection schemes can be classified as extra-injection, using two or three colliding laser beams [14, 15, 20]; and self-injection, which consists of a self-modulated LWFA (SMLWFA) [7, 11, 12, 17, 18], wave breaking injection [9, 13], and beam loading in the bubble regime [16, 19, 21-24].

As for the diagnostic of laser wakefield, the first measurements of temporal and spatial characteristics of LWF were reported [25, 26]. These measurements were based on the phase shift of the co-propagating ultra short ($\tau_L < \tau_p$) probe pulses using frequency-domain interferometry (FDI) technique. Another diagnostic method especially feasible for measuring large amplitude LWF is based on the photon acceleration technique (frequency shift) [27]. In both above techniques, it is necessary to control the relative delay time of the probe pulses and wakefield to locate the short probe pulse at a proper phase of the wakefield. In a highly relativistic case, the steepening and wavebreaking of wakefileds appear because of strong relativistic nonlinear effects [28-30]. Probe laser pulse can neither be short enough nor be located precisely.

It has been well known that the pump laser light is scattered as stimulated Raman scattering, when it interacts with the plasma strongly. It is a kind of resonant three wave coupling between electromagnetic wave and plasma wave. It is the key issue for the self-phase modulated laser wakefield acceleration [7, 11, 17], and can be used as a

diagnostic tool for the measurement of wakefield [12, 18]. And the forward stimulated Raman scattering light can be cross-phase modulated (RXPM) by the pump laser while co-propagating in the plasma [31]. And it can be used as a diagnostic tool in the laser-plasma interaction.

The technique using small-angle coherent Thomson Scattering of a co-propagating probe pulse to measure the temporal evolution of the plasma wakefiled has been reported theoretically [32] and experimentally [33, 34]. The scattering intensity of probe pulse is obtained by the Born approximation [32], $P_s = \tilde{n}^2 r_0^2 \lambda_0^2 L_g^2 P_0 / 4$, where $\tilde{n}$ is the density perturbation of plasma wave, r_0 is the classical electron radius $e^2 / m_e c^2$, λ_0 is the wavelength of the incident probe pulse, L_g is the interaction distance, and P_0 is the incident power. However, theoretical analysis is mainly about the side scattering, namely, the wave vectors of fluctuations are oriented nearly perpendicular to the wave number of incident probe laser. While in the experiments [34], the probe lasers are parallel to the wakefield. Above formula may be applicable also to forward scattering, however, the detail analysis on the forward scattering was not done in this analysis.

At the same time, above formula is derived from the fact that the plasma density fluctuation is monochromatic. While in the nonlinear or relativistic region, the multiple sidebands appear in the spectra of both pump laser [11, 12, 18] and probe laser pulse [34]. These multiple sidebands are related to the nonlinear steepening of density perturbation of wakefield [35]. The amplitude of sidebands in the spectrum of pump laser has been obtained [36]. As for the probe pulse, only total scattering intensity of monochromatic density fluctuation is given [32] or relative amplitude of sidebands is obtained by harmonic wave analysis [35]. In this paper, we deduce the analytical solution for relation of nonlinear evolution of laser wakefield to the multiple sidebands of forward Raman scattering of a co-propagating, relatively weak and long probe pulse. This analytical solution is consistent with the particle-in-cell simulations and above experiments. It is possible to measure the steepening of wakefields with this correlation.

3.2. Basic equations

When an intense laser light propagates inside a plasma, the relativistic dispersion relation $\omega_0^2 = \omega_{p0}^2 / \gamma_0 + c^2 k_0^2$ is satisfied, where ω_{p0} is the plasma frequency associated with the zeroth-order electron density $\omega_{p0}^2 = 4\pi e^2 n_0 / m_e$,

$\gamma_0 = \left[1+\left(p_0/m_e c\right)^2\right]^{1/2}$ is the relativistic factor associated with LWF and laser amplitude where $p_0/m_e c$ is the average longitudinal momentum $\left\langle \left(p_{//}/m_e c\right)^2 \right\rangle = a_0^2/2$. Laser group velocity, namely the propagation velocity of wave envelope is obtained from above dispersion relation to be $v_g = c(1-n_0/\gamma_0 n_c)^{1/2}$, here n_c is the plasma critical density which is the maximum density for the propagation of a light wave with frequency ω_0 for $\gamma_0 = 1$. For the analysis, we introduce an algebraic transformation of space and time variables from laboratory frame to a frame moving with the group velocity of pump laser pulse. In this 'co-moving' frame, where $\xi = x - v_g t$, $\tau = t$, light pulse is considered to be stationary. So if the pump laser pulse is short sufficiently, the plasma can be assumed to be varying slowly with time τ, namely $\partial/\partial\tau \ll \partial/\partial\xi$. Under this quasi-static assumption, derived from the equation of electron motion and the Maxwell's equations, the nonlinear 1D governing equation for the wake potential [3] is given by

$$\frac{\partial^2\phi}{\partial\xi^2} = -k_p^2\gamma_g^2\left\{1-\frac{\beta_g(1+\phi)}{[(1+\phi)^2-\gamma_g^{-2}(1+a^2)]^{1/2}}\right\} \tag{3.1}$$

where $\phi = e\Phi/m_e c^2$ is the normalized electrostatic potential, k_p is the wave number of plasma wave, $a = e\mathbf{A}/m_e c^2$ is the normalized transverse vector potential of pump laser, $\beta_g = v_g/c$ and $\gamma_g = (1-\beta_g^2)^{-1/2}$. Eq. (3.1) can be integrated numerically for any given pump laser.

To diagnose the amplitude and wavelength of wakefield plasma wave, a relatively long and weak probe pulse is injected into the wake. As the amplitude of probe pulse is much lower than that of the pump pulse, the wakefield is not affected by the probe laser. However, the probe laser light is modulated by density fluctuations associated with wakefield. The wave equation describing the propagation of probe light in the wake is given by

$$\left(\frac{\partial^2}{\partial t^2} - c^2\frac{\partial^2}{\partial x^2}\right)\mathbf{a}(x,t) = -\omega_{p0}^2\frac{n_e(x,t)}{\gamma(x,t)n_0}\mathbf{a}(x,t) \tag{3.2}$$

where $\mathbf{a}(x,t)$ is the normalized transverse vector potential of the probe light, $\gamma(x,t)$ is the relativistic factor of electrons. $n_e(x,t)$ is the local electron density of plasma. We introduce an envelope function of the probe laser $b(x,t)$ by $\mathbf{a}(x,t) = \mathbf{b}(x,t)\exp[i(k_0 x - \omega_0 t)]$, where k_0 and ω_0 are the wave number and frequency of probe pulse in the ambient plasma that satisfy the dispersion relation, namely $k_0/\omega_0 = v_g/c^2$. In the following analysis, we introduce a frame which

co-moves with the wakefield, namely with the velocity of v_g. Then the wave envelope equation becomes

$$[\frac{\partial^2}{\partial\tau^2}-\frac{c^2}{\gamma_g^2}\frac{\partial^2}{\partial\xi^2}-2v_g\frac{\partial^2}{\partial\xi\partial\tau}-2i\omega_0\frac{\partial}{\partial\tau}]b(\xi,\tau)=-\omega_{p0}^2\delta(n_e/\gamma n_0)b(\xi,\tau) \qquad (3.3)$$

Here, we assume that the amplitude and profile of the wakefield and the envelope of the pump laser pulse are stationary. Then, the amplitude $b(\xi,\tau)$ of the probe pulse is varying slowly, so the second order of time derivative can be neglected. $\delta(n_e/n_0\gamma)=n_e/n_0\gamma-1$ is the perturbation of plasma wave. The wave envelope in Eq. (3.3) can be divided into a fundamental light and scattered ones as $b(\xi,\tau)=b_0(\xi,\tau)+b_s(\xi,\tau)$. Since the scattered lights grow through the wakefield and the probe laser interaction, the amplitudes are assumed much smaller than the amplitude of the incident laser, namely, $b_s<<b_0$. Under these conditions, Eq. (3.3) is reduced to

$$[\frac{c^2}{\gamma_g^2}\frac{\partial^2}{\partial\xi^2}+2v_g\frac{\partial^2}{\partial\xi\partial\tau}+2i\omega_0\frac{\partial}{\partial\tau}]b_s(\xi,\tau)=\omega_{p0}^2\delta(n_e/n_0\gamma)b_0(\xi,\tau) \qquad (3.4)$$

When the amplitude of wake wave is stationary, the wakefield amplitude depends only on ξ. In this case, the nonlinear wakefield amplitude can be expressed by

$$\delta(n_e/n_0\gamma)=\sum_l N(l)\exp[ilk_p\xi] \qquad (3.5)$$

where k_p is the fundamental wake field wave number, and $N(l)$ is the lth higher harmonic of $\delta(n_e/n_0\gamma)$ which corresponds to the steepening of the wakefield.

We also decompose the scattered lights into Fourier components as follows

$$b_s(\xi,\tau)=\sum_l b_l(\tau)\exp[ilk_p\xi] \qquad (3.6)$$

here $b_l(\tau)$ is the Fourier function of the scattered probe wave envelope. For simplicity, we neglect the ξ dependence of $b_l(\tau)$. We substitute Eqs. (3.5) and (3.6) into Eq. (3.4) to obtain

$$[-\frac{l^2c^2k_p^2}{\gamma_g^2}+2i(\omega_0+lv_gk_p)\frac{\partial}{\partial\tau}]b_l(\tau)=\omega_{p0}^2N(l)b_0(\tau) \qquad (3.7)$$

When $|N(l)\omega_{p0}^2\gamma_g^2/l^2c^2k_p^2|\gg|b_l(\tau)/b_0(\tau)|$, Eq. (3.7) is reduced to

$$\frac{\partial}{\partial \tau} b_l(\tau) = \frac{-i\omega_{p0}^2 N(l) b_0(\tau)}{2(\omega_0 + l\omega_p)} \tag{3.8}$$

by neglecting the first term of Eq. (3.7) and using the relationship $\omega_p = k_p v_g$, when $b_s << b_0$, we can assume $b_0(\tau) \approx b_0$ is constant, so that Eq. (3.8) can be integrated to obtain

$$b_l(\tau) = -\frac{i\omega_{p0}^2 N(l) b_0 L_g}{2(\omega_0 + l\omega_p) v_g} \tag{3.9}$$

here $L_g = v_g \tau$ is the propagation distance of the probe laser light. Eq. (3.9) indicates that the lth scattered probe light is proportional to the propagation distance L_g and the lth harmonic amplitude $N(l)$ of the wakefield. This formula shows that the wakefield profile, $N(\xi) = \sum_l N(l) \exp[ilk_p \xi]$, can be determined when the Raman sidebands spectrum $b_l(\tau)$ is obtained.

Assumed that $l\omega_p << \omega_0$, the analytical solution Eq. (3.9) is consistent with Slusher's [32] which is under the assumption that the probe pulse is scattered from a monochromatic density fluctuation $n(r,t) = \tilde{n}\cos(K_0 x - \Omega t + \eta)$, where K_0 is the wave number, Ω is the frequency of plasma, and η is a time independent phase. Compared with Slusher's solution of scattering intensity, Eq. (3.9) supplies: first, finer structure of scattering spectrum with factor $l\omega_p$; second, the correlation of high harmonics of scattering and steepening of density perturbation which happens in the relativistic or nonlinear regime.

Next we can compare the analytical solution with the harmonic wave analysis. In Blanc's paper [34], the ratio of second harmonic plasma wave to first one is $\delta n_2 / \delta n_1 \approx 0.1$, and the ratio of second scattering satellite to first one is $P_2 / P_1 \approx 0.01$, which is consistent with Eq. (3.9) $P_2 / P_1 = b_2^2 / b_1^2 = N_2^2 / N_1^2$.

By using the second order approximation, we can derive the amplitude depletion of the incident probe light by using Eq. (3.3). Namely, the $l = 0$ mode, $b_0(\tau)$ subjects to

$$2i\omega_0 \frac{\partial}{\partial \tau} b_0(\tau) = \omega_{p0}^2 \sum_{l=\pm 1}^{\pm\infty} N(l) b_{-l}(\tau) \tag{3.10}$$

By substituting Eq. (3.9) into Eq. (3.10), we obtain

$$b_0(\tau) = b_0 - \sum_{l=\pm 1}^{\pm\infty} \frac{\omega_{p0}^4}{8\omega_0(\omega_0 + l\omega_p)} \frac{L_g^2}{v_g^2} |N(l)|^2 \tag{3.11}$$

Eq. (3.11) indicates that the depletion of the incident probe beam is proportional to the mean square of the wakefield amplitude approximately.

3.3. PIC Simulations

PIC simulations are exploited to confirm the validation of the above formulas. Because both the excitation of wake wave and Raman scattering are one-dimensional (1D) effects, here 1D fully relativistic and electromagnetic PIC code is used. In the simulations the total length is $500\lambda_0$, the cell size is $0.05\lambda_0$ and the time step is $0.05\tau_0$, where λ_0 and τ_0 are the wavelength and the period of the pump laser. Homogeneous plasma is located at the center of the simulation box with length of $L_g = 200\lambda_0 - 400\lambda_0$. In each cell 20 simulation particles representing electrons are placed and ions are fixed as immobile background. For typical laser wakefield acceleration, the plasma density $n_e = 10^{18} - 10^{19}$ cm^{-3}. The critical plasma density $n_c = 1.1\times10^{21}$ cm^{-3} for $\lambda_0 = 1$ μm. So in the simulations, we set the plasma density $2.5\times10^{-3} n_c - 1.0\times10^{-2} n_c$ to correspond the typical laser wakefield cases. The incident pump laser is linearly polarized, and has longitudinal profile $a = a_0 \sin(\pi x / L)$, where $a_0 = \sqrt{I\lambda_0^2 / 1.38\times10^{18}}$ is the normalized vector potential , and L is the laser duration. The laser intensity in the generation of laser wakefield is the order of 10^{18} w/cm^2. So the normalized vector potential used in the simulations ranges $a_0 = 0.5 - 2.2$. To excite the wakefield maximally, the laser duration is required to equal to the plasma wavelength ($L \approx \lambda_p$) [2]. The laser durations are set to satisfy this requirement for various plasma densities in the simulations. For the diagnostic of wakefield, a probe laser pulse is injected behind the pump laser. The probe laser pulse has the same polarization with the pump laser. But the frequency of the probe laser is doubled to make the spectral measurement in experiments easier and the Eq. (3.9) valid longer. It is required that the probe laser light is relatively long and weak compared with the pump laser. So in the longitudinal space, the probe laser rises up in $10\lambda_0$, maintains its peak amplitude $b_0 = 0.05$ for $80\lambda_0$, and falls down in $10\lambda_0$. In this scheme, the location of the probe laser is not required to be controlled precisely in comparison with other schemes. In all simulations, the interval between the pump laser and the probe laser is fixed at $10\lambda_0$.

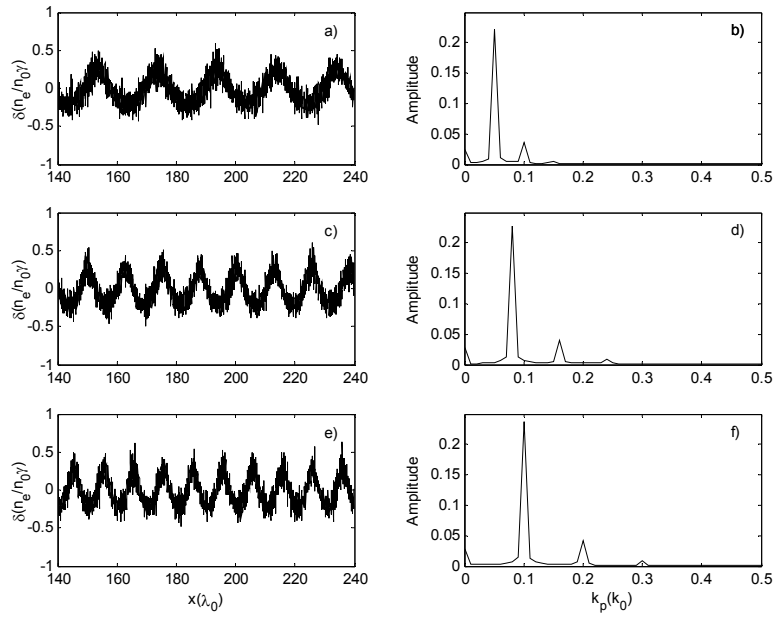

Fig. 3.1. Profiles and spectra of plasma oscillation when the pump lasers arrive at $280\lambda_0$ for pump laser $a_0 = 0.8$, with plasma density a) and b) $n_e = 2.5\times10^{-3} n_c$, c) and d) $n_e = 6.4\times10^{-3} n_c$, e) and f) $n_e = 1.0\times10^{-2} n_c$.

In the first series of simulations, plasma length is fixed as $L_g = 300\lambda_0$, but the densities are varied as $2.5\times10^{-3} n_c$, $6.4\times10^{-3} n_c$ and $1.0\times10^{-2} n_c$ corresponding to the plasma wavelength of $20\lambda_0$, $12.5\lambda_0$ and $10\lambda_0$. So the durations of the pump lasers are adjusted to the corresponding values, but the intensities are all kept at $a_0 = 0.8$. Fig. 3.1 plots the profiles and the spectra of the plasma oscillation $\delta(n_e / n_0\gamma)$ in the first series while the pump lasers arrive at $280\lambda_0$. It is shown that wavelengths of the wakefields are well consistent with the expectation $k_p = \sqrt{4\pi e^2 n_0 / m_e c^2}$. In the first series, the intensities of the pump laser are the same. From nonlinear plasma theory, it is derived that the amplitude of the wakefield is correlated to the pump laser intensity. So the amplitudes of the wakefields in the first series are the same, which is elucidated in Fig. 3.1.

Fig. 3.2 shows the spectra of the probe laser light after propagating through $300\lambda_0$. As expected from Eq. (3.9), the multiple sidebands around the fundamental frequency appear. The frequency shift between the lth sideband and the fundamental is $l\omega_p$. The amplitudes of the first up-shifted anti-Stokes and down-shifted Stokes are the strongest since they represent the fundamental components of wakefields, but signals of the second and third sidebands are also observed. Besides the amplitude of wake field, the amplitude of the scattered probe laser light is proportional to the

plasma frequency. So, by comparing three cases in the first series, it is found that the amplitudes of sidebands are higher, for higher plasma density and higher plasma frequency.

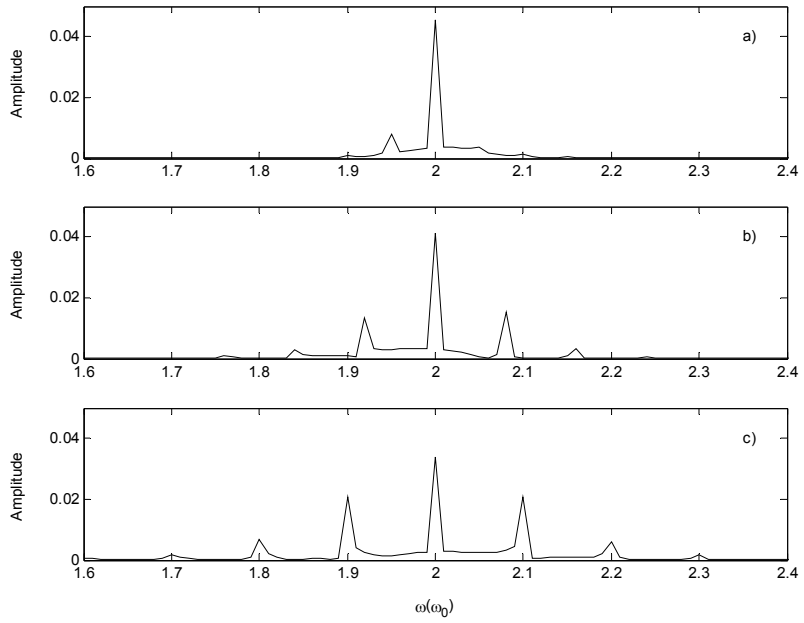

Fig. 3.2. Spectra of probe laser lights after co-propagating with wakefield of $300\lambda_0$ for pump laser $a_0 = 0.8$, with plasma density a) $n_e = 2.5\times10^{-3} n_c$, b) $n_e = 6.4\times10^{-3} n_c$, c) $n_e = 1.0\times10^{-2} n_c$.

In the second series of simulations, plasma density is fixed at $6.4\times10^{-3} n_c$, the pulse width of the pump lasers is fixed as $L = 12.5\lambda_0$, but pump laser intensities are varied as $a_0 = 0.5$, 0.8 and 1.0. When the pump laser intensity is low enough and has a sine-profile, Eq. (3.1) can be analytically solved to obtain the wakefield potential ϕ behind the pump laser ($\xi \le 0$) [2]

$$\phi(\xi) = \frac{2\pi^2 \Phi_L}{4\pi^2 - k_p^2 \xi_L^2}\left[\cos k_p(\xi - \xi_L) - \cos k_p \xi\right] \tag{3.12}$$

where $\Phi_L = -a_0^2/2$ is the normalized ponderomotive potential of pump laser. The profile and spectrum of the wake field for $a_0 = 0.5$ shown in Fig. 3.3 a) and b). It is shown the wake field is monochromic with wavelength k_p. So in the spectrum of the probe laser, see Fig. 3.4 a), only first anti-Stokes and Stokes are observed.

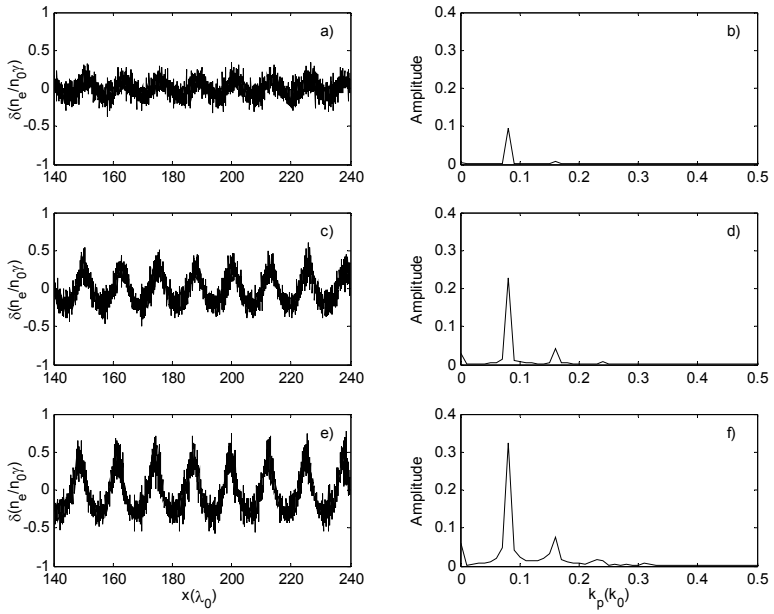

Fig. 3.3. Profiles and spectra of plasma oscillation when the pump lasers arrive at $280\lambda_0$ for plasma density $n_e = 6.4\times10^{-3} n_c$, with pump laser a) and b) $a_0 = 0.5$, c) and d) $a_0 = 0.8$, e) and f) $a_0 = 1.0$.

When pump laser strength increases to be relativistic $a_0 \sim 1.0$, relativistic nonlinear effects become important. Then the waveform of the wake field is steepened, which corresponds to the generation of high harmonics in the spectrum of the wakefield [7]. These phenomena are observed in the profiles and spectra of the wakefield for $a_0 = 0.8$ and 1.0 cases, see Fig. 3.3 b) – f). It is shown that for the higher pump laser intensity, the wake field amplitudes are higher, since the amplitude of wakefield is proportional to the pump laser intensity. Since the amplitude of higher *lth* modes becomes significant, we should retain the first term of RHS of Eq. (3.7) to obtain

$$b_l(\tau) = \frac{\omega_{p0}^2 N(l)}{2i(\omega_0 + l v_g k_p)} \int_0^\tau b_0(s)\, \mathrm{e}^{\frac{l^2 c^2 k_p^2 (\tau - s)}{2i(\omega_0 + l v_g k_p)\gamma_g^2}} ds \tag{3.14}$$

And the amplitude of sidebands of scattered lights can be obtained when b_0 is assumed constant.

$$b_l(\tau) = \frac{\omega_{p0}^2 N(l) \gamma_g^2 b_0}{l^2 c^2 k_p^2} \left[1 - \mathrm{e}^{\frac{l^2 c^2 k_p^2 \tau}{2i(\omega_0 + l v_g k_p)\gamma_g^2}} \right] \tag{3.15}$$

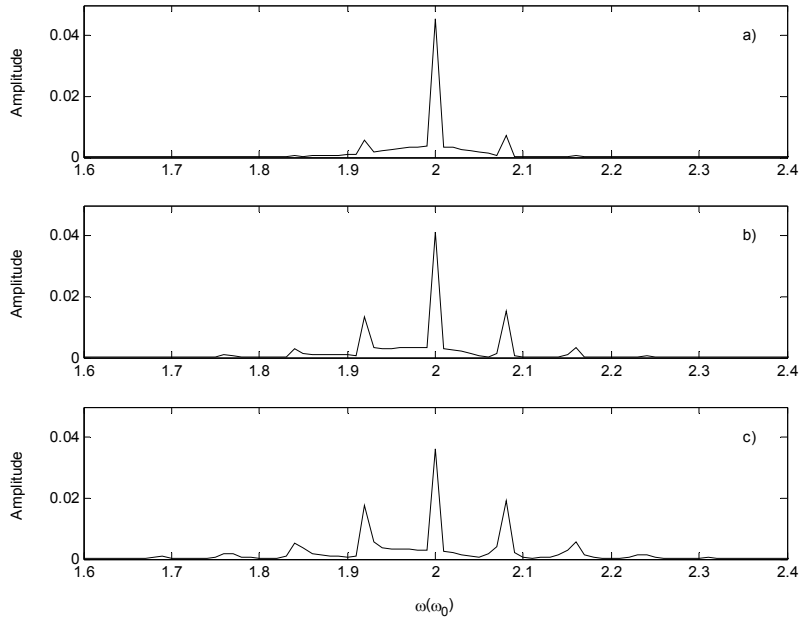

Fig. 3.4. Spectra of probe laser lights after co-propagating with wakefield of $300\lambda_0$ for plasma density $n_e = 6.4\times10^{-3} n_c$, with pump laser a) $a_0 = 0.5$, b) $a_0 = 0.8$, c) $a_0 = 1.0$.

Spectra of the probe laser light in this series are plotted in Fig. 3.4. The excitation of sidebands of probe light around the initial laser peak $2\omega_0$ is observed. The relation between the sidebands amplitudes of the probe laser light and the wake field spectrum agrees well with that predicted by the Eq. (3.9).

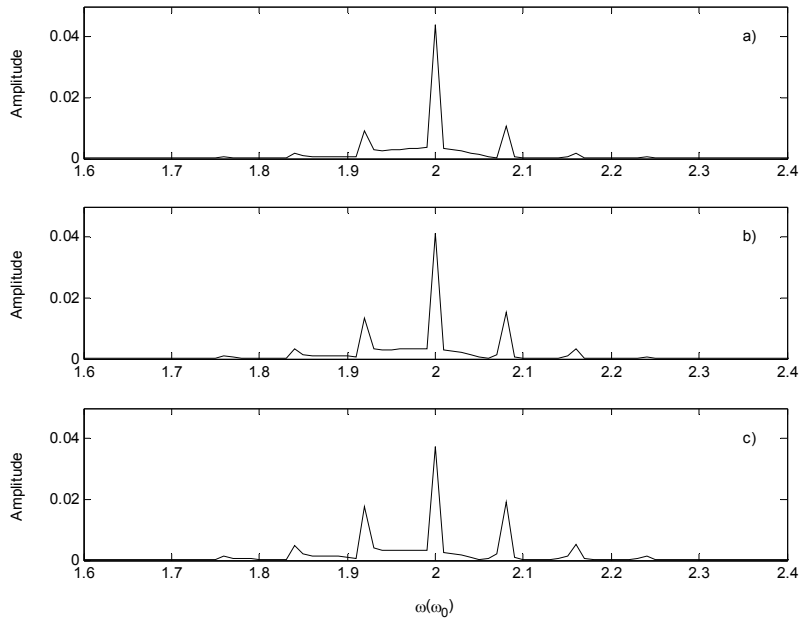

Fig. 3.5. Spectra of probe laser lights for pump laser $a_0 = 0.8$ and plasma density

$n_e = 6.4\times10^{-3} n_c$ after co-propagating with wakefield of a) $L_g = 200\lambda_0$, b) $L_g = 300\lambda_0$ and c) $L_g = 400\lambda_0$.

Since sideband amplitude of the scattered probe laser is proportional to the propagation distance, in the third series of simulations, we keep $n_e = 6.4\times10^{-3} n_c$, $L = 12.5\lambda_0$, and $a_0 = 0.8$, then measure the probe laser after propagating through $L_g = 200\lambda_0$, $300\lambda_0$ and $400\lambda_0$. The spectra of the probe laser measured at the different propagation distances are shown in Fig. 3.5 and agree well with those obtained by the Eq. (3.9).

Table 3.1. Parameters and results of PIC simulations

a_0	0.8	0.8	0.8	0.5	1.0	0.8	0.8
$n_0(n_c)$	0.0025	0.0064	0.01	0.0064	0.0064	0.0064	0.0064
$L_g(\lambda_0)$	300.0	300.0	300.0	300.0	300.0	200.0	400.0
$N_1(\omega_p)$	0.2228	0.2395	0.2699	0.0951	0.3505	0.2299	0.2552
$N_2(\omega_p)$	0.2219	0.2269	0.2395	0.0959	0.3169	0.2269	0.2269
Error(%)	0.4	5.4	11.9	0.9	10.0	1.3	11.7

Therefore, if the spectrum of the probe laser is measured, the plasma wake field amplitude and the structure factor can be determined from the Eq. (3.9). All parameters in the above three series of simulation are plotted in table 1. $b(2\omega_0)$ and $b(2\omega_0+\omega_p)$ are the amplitudes of the fundamental component and first sideband of the probe laser light. Substituting these parameters into Eq. (3.9), the amplitude of the fundamental component of wakefield $N_1(\omega_p)$ is obtained by using Eq. (3.9). $N_2(\omega_p)$ is the amplitude of the fundamental component of wakefield measured directly in the PIC simulation. The maximum error of these two values is 11.9%. It can be concluded that this probing method is applicable to measuring the laser wake field structure from the laser scattering data. Data of higher harmonics are not listed in the table, but it was also checked that they agree well with the predicted values of the

Eq. (3.9).

It is widely recognized that the most promising application of the LWF is laser accelerator. To see the influence of trapped and accelerated electrons to the probe laser light, we simulated a series of cases in which electrons are well trapped and accelerated by wakefields but with different injection schemes. In this series, parameters of probe laser are as the same as previous series, but pump laser and plasma densities are varied case by case according to the corresponding injection scheme.

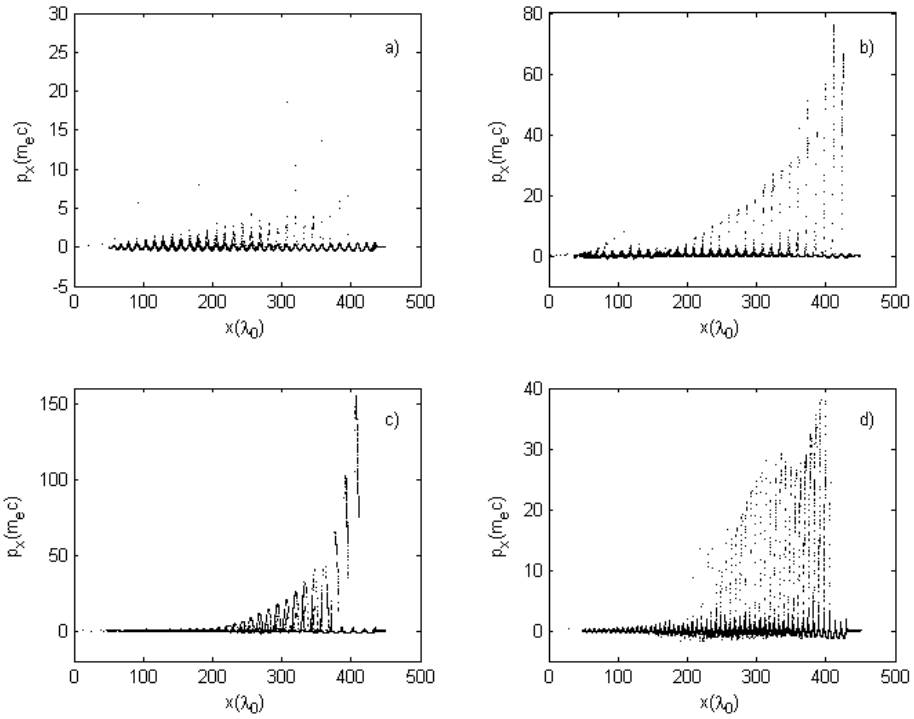

Fig. 3.6. Electron distributions in phase space for scheme a) without electron injection, b) with electron injection via colliding lasers, c) with electron injection via wave breaking and d) with electron injection via SMLWFA.

First, we simulate a case without trapping and acceleration of electrons. In this case, plasma density is $6.4\times10^{-3}n_c$ and the length of plasma region is $400\lambda_0$. The amplitude of pump laser is $a_0=1.2$, and the pulse width is $L=12.5\lambda_0$. The electron distribution in p_x-x phase space when the front of pump laser arrives at $x=440\lambda_0$ is plotted in Fig. 3.6 a) which shows that there is no electron injected and trapped, although nearly wave breaking occurs. And the corresponding spectrum of the probe laser light is shown in Fig. 3.7 a).

In the second case, extra-injection via two colliding laser pulses [14, 15, 20] is simulated. Parameters of plasma and pump laser are as the same as in the first case. Besides the pump laser, there is a counter-propagating laser pulse with same frequency, polarization and duration of the pump laser. Amplitude of the counter laser is 0.4. The two laser pulses collide at $x = 100\lambda_0$ and the colliding laser pulse injects electrons into wake field. In the third simulation, plasma parameters are kept as previous case, but amplitude of the pump laser is increased to $a_0 = 2.2$. In this highly relativistic intensity regime, the seed electrons can be self-injected into the wake field by the wave breaking [9, 13]. This case is called the Self-Injection WFA (SIWFA). The last case of this series is the simulation of injection scheme via SMLWFA [7, 11, 12, 17, 18]. In this scheme, plasma density is higher than the plasma density satisfying $\lambda_p \approx L$. So plasma density in this case is adjusted to $2.0\times10^{-2} n_c$, and other parameters are kept as the same as in the first case of this series.

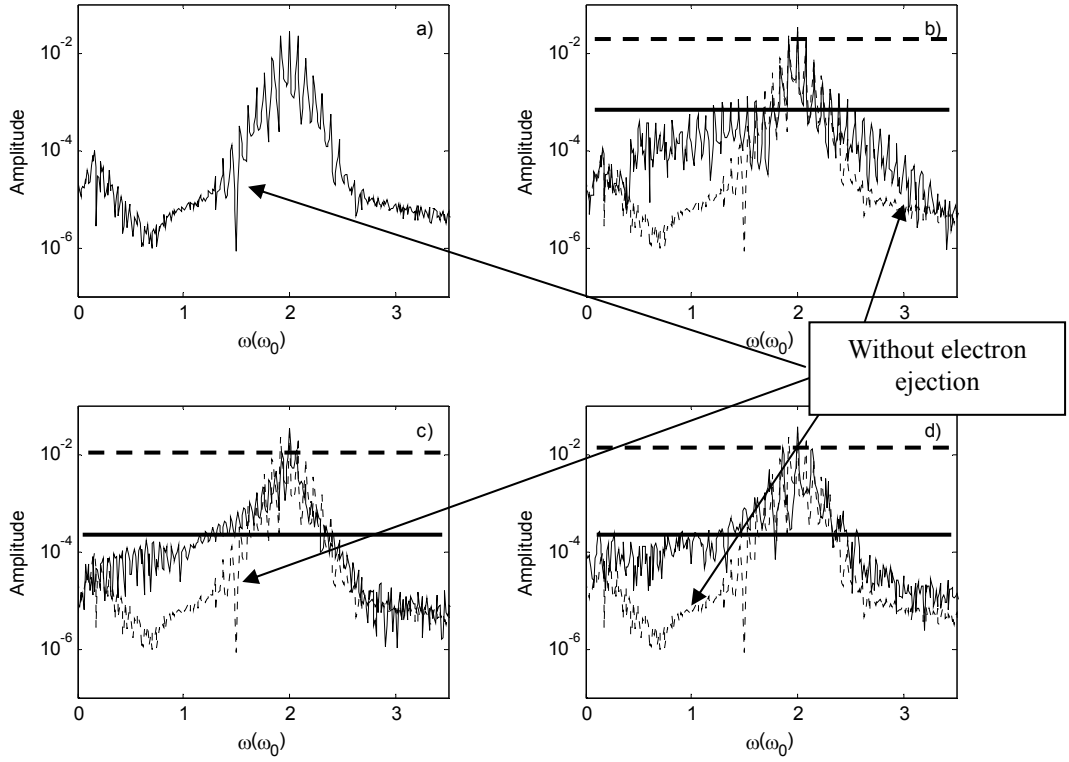

Fig. 3.7. a) spectrum of probe laser light for scheme without electron injection, spectrum of probe laser light (solid line) for scheme b) with electron injection via colliding lasers, c) with electron injection via wave breaking and d) with electron injection via SMLWFA and scheme without electron injection (dotted line).

Electron distributions in $p_x - x$ phase space of the last three cases are plotted in Figs. 3.6 b) – d). We can see that these schemes are efficient for the trapping and acceleration of electrons. From Fig. 3.7 b) – d), we can see clearly by comparing Fig. 3.7(a) and Fig. 3.7 (b),(c),(d) that there are wide wings in the spectrum of the scattered probe laser. In the case of electrons are trapped and accelerated, plasma density $N(l) = N_p(l) + N_b(l)$, where $N_b(l)$ is the distribution from trapped and accelerated bunch electrons, and $N_p(l)$ is the distribution of background electron plasma wave. These wings corresponds to the laser scattering by narrow electron bunches, namely the contribution of $N_b(l)$. Formation of the wings is similar in the spectrum of the pump laser due to stimulated Raman scattering when wave breaking occurs [11]. In our paper, the wing structure of the probe light is due to the electrons trapped and accelerated by wake field.

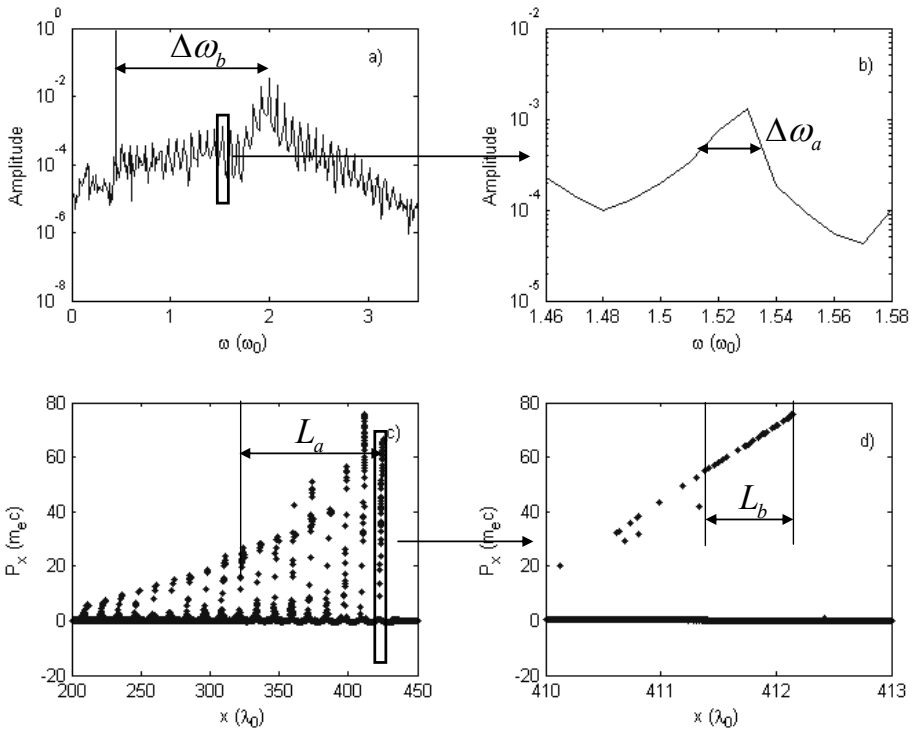

Fig. 3.8 a) Spectrum of probe laser light, b) Zoom in of the square in a), c) Electron distribution in phase space, d) zoom in of the square in c) with electron injection via colliding lasers

See Fig. 3.8, the width of the wing ($\Delta\omega_b$) is inversely proportional to the bunch width in one wake field potential well (L_b) as $L_b = 2\pi c/\Delta\omega_b$. Since the wing extends to $\pm 20\omega_p$, the bunch width can be determined to be $\omega_p/20$ from the spectrum. On the

other hand, the width of each sideband ($\Delta\omega_a$) is inversely proportional to the length where effective trapping and acceleration happen (L_a) as $L_a=2\pi c/\Delta\omega_a$. Here the width of sideband is about $\lambda_p/10$, so the effective accelerating length can be determined to be $10\lambda_p$.

The wing structures are different between the Fig. 3.7 b) and the Fig. 3.7 c) and d). The difference is in two ways. One is the relative amplitude of the wing (a solid horizontal line) to the first harmonics (broken horizontal line) is higher for the counter laser injection (Fig. 3.7 b)) by 2 times than the other two schemes (Fig. 3.7 c) and d)). This indicates that the number of injected electron relative to the wake field density fluctuation for the counter laser injection is two times higher than those for the other cases. As the consequence of this result, the Eq. (3.9) can be used for determining the total bunch electron charge from the scattered laser spectrum.

Each side band spectrum in the wing of the Fig. 3.7 b) is narrower than those for the Fig. 3.7 c) and d). This indicates that the number of bunch is larger for the counter laser injection than for the SIWFA. When the line width of one side band line is $\Delta\omega$, the number of bunch is estimated to be $\omega_p/\Delta\omega$.

3.4. Conclusion

In this chapter, 1D simulation results and an analytical solution for the multiple sidebands of a probe laser pulse which is scattered by the wakefield are presented. These results can be used as a diagnostic tool for the wakefield. The convenience of this scheme is that the interval between the pump laser pulse and the probe laser pulse is not required to be controlled precisely in comparison with the other schemes, where the probe laser pulse width is shorter than the wakefield period and the probe pulse should be injected at a given phase of the wake-filed. In the scheme of this chapter, since the probe laser pulse is longer than the wake-filed wavelength, the accuracy of the injection timing could be a few wake-filed wavelengths.

In the present scheme, the spectrum of the multiple sidebands can provide much detailed information about the wakefield by using the proposed analytical formula based upon 1D PIC simulations. The scheme of this paper is similar to the scheme that was discussed in a phenomenological way in the Ref. 34. The PIC simulations and the analytical results of this paper are consistent with the results of the experiment in Ref. 34.

On the other hand, it is found that the wing structure in the scattered probe laser

spectrum is useful for diagnosing the trapping and accelerating of electron bunches. Hence, it can be concluded that this diagnostic can be employed to measure laser wake field for a large parameter range of plasma density, plasma length and pump laser amplitude.

Reference

1. Tajima, T. and J.M. Dawson, *Laser Electron Accelerator.* Physical Review Letters, 1979. **43**(4): p. 267.

2. Sprangle, P., et al., *Laser wakefield acceleration and relativistic optical guiding.* Applied Physics Letters, 1988. **53**(22): p. 2146-2148.

3. Sprangle, P., E. Esarey, and A. Ting, *Nonlinear theory of intense laser-plasma interactions.* Physical Review Letters, 1990. **64**(17): p. 2011.

4. Sprangle, P., et al., *Propagation and guiding of intense laser pulses in plasmas.* Physical Review Letters, 1992. **69**(15): p. 2200.

5. Antonsen, T.M. and P. Mora, *Self-focusing and Raman scattering of laser pulses in tenuous plasmas.* Physical Review Letters, 1992. **69**(15): p. 2204.

6. Esarey, E., J. Krall, and P. Sprangle, *Envelope analysis of intense laser pulse self-modulation in plasmas.* Physical Review Letters, 1994. **72**(18): p. 2887.

7. Esarey, E., et al., *Trapping and Acceleration in Self-Modulated Laser Wakefields.* Physical Review Letters, 1998. **80**(25): p. 5552.

8. Mori, W.B., et al., *Evolution of self-focusing of intense electromagnetic waves in plasma.* Physical Review Letters, 1988. **60**(13): p. 1298.

9. Tzeng, K.C., W.B. Mori, and T. Katsouleas, *Electron Beam Characteristics from Laser-Driven Wave Breaking.* Physical Review Letters, 1997. **79**(26): p. 5258.

10. Tsung, F.S., et al., *Near-GeV-Energy Laser-Wakefield Acceleration of Self-Injected Electrons in a Centimeter-Scale Plasma Channel.* Physical Review Letters, 2004. **93**(18): p. 185002.

11. Modena, A., et al., *Electron acceleration from the breaking of relativistic plasma waves.* Nature, 1995. **377**(6550): p. 606-608.

12. Umstadter, D., et al., *Nonlinear Optics in Relativistic Plasmas and Laser Wake Field Acceleration of Electrons.* Science, 1996. **273**(5274): p. 472-475.

13. Malka, V., et al., *Electron Acceleration by a Wake Field Forced by an Intense Ultrashort Laser Pulse.* Science, 2002. **298**(5598): p. 1596-1600.

14. Umstadter, D., J.K. Kim, and E. Dodd, *Laser Injection of Ultrashort Electron Pulses into Wakefield Plasma Waves.* Physical Review Letters, 1996. **76**(12): p. 2073.

15. Esarey, E., et al., *Electron Injection into Plasma Wakefields by Colliding Laser Pulses.* Physical Review Letters, 1997. **79**(14): p. 2682.

16. Pukhov, A. and J. Meyer-ter-Vehn, *Laser wake field acceleration: the highly*

non-linear broken-wave regime. Applied Physics B: Lasers and Optics, 2002. **74**(4): p. 355-361.

17. Nakajima, K., et al., *Observation of Ultrahigh Gradient Electron Acceleration by a Self-Modulated Intense Short Laser Pulse.* Physical Review Letters, 1995. **74**(22): p. 4428.

18. Coverdale, C.A., et al., *Propagation of Intense Subpicosecond Laser Pulses through Underdense Plasmas.* Physical Review Letters, 1995. **74**(23): p. 4659.

19. Moore, C.I., et al., *Electron Trapping in Self-Modulated Laser Wakefields by Raman Backscatter.* Physical Review Letters, 1997. **79**(20): p. 3909.

20. Faure, J., et al., *Controlled injection and acceleration of electrons in plasma wakefields by colliding laser pulses.* Nature, 2006. **444**(7120): p. 737-739.

21. Mangles, S.P.D., et al., *Monoenergetic beams of relativistic electrons from intense laser-plasma interactions.* Nature, 2004. **431**(7008): p. 535-538.

22. Geddes, C.G.R., et al., *High-quality electron beams from a laser wakefield accelerator using plasma-channel guiding.* Nature, 2004. **431**(7008): p. 538-541.

23. Faure, J., et al., *A laser-plasma accelerator producing monoenergetic electron beams.* Nature, 2004. **431**(7008): p. 541-544.

24. Chang, C.L., et al., *Production of a monoenergetic electron bunch in a self-injected laser-wakefield accelerator.* Physical Review E, 2007. **75**(3): p. 036402-10.

25. Marques, J.R., et al., *Temporal and Spatial Measurements of the Electron Density Perturbation Produced in the Wake of an Ultrashort Laser Pulse.* Physical Review Letters, 1996. **76**(19): p. 3566.

26. Siders, C.W., et al., *Laser Wakefield Excitation and Measurement by Femtosecond Longitudinal Interferometry.* Physical Review Letters, 1996. **76**(19): p. 3570.

27. Dias, J.M., L. Oliveira e Silva, and J.T. Mendonca, *Photon acceleration versus frequency-domain interferometry for laser wakefield diagnostics.* Physical Review Special Topics - Accelerators and Beams, 1998. **1**(3): p. 031301.

28. Dawson, J.M., *Nonlinear Electron Oscillations in a Cold Plasma.* Physical Review, 1959. **113**(2): p. 383.

29. Jackson, E.A., *Nonlinear Oscillations in a Cold Plasma.* Physics of Fluids, 1960. **3**(5): p. 831-833.

30. Koch, P. and J. Albritton, *Nonlinear Evolution of Stimulated Raman Backscatter*

in Cold Homogeneous Plasma. Physical Review Letters, 1975. **34**(26): p. 1616.

31. Chen, S., et al., *Observation of relativistic cross-phase modulation in high-intensity laser-plasma interactions.* Physical Review E, 2006. **74**(4): p. 046406-6.

32. Slusher, R.E. and C.M. Surko, *Study of density fluctuations in plasmas by small-angle CO_2 laser scattering.* Physics of Fluids, 1980. **23**(3): p. 472-490.

33. Ting, A., et al., *Temporal Evolution of Self-Modulated Laser Wakefields Measured by Coherent Thomson Scattering.* Physical Review Letters, 1996. **77**(27): p. 5377.

34. Le Blanc, S.P., et al., *Temporal Characterization of a Self-Modulated Laser Wakefield.* Physical Review Letters, 1996. **77**(27): p. 5381.

35. Umstadter, D., et al., *Observation of steepening in electron plasma waves driven by stimulated Raman backscattering.* Physical Review Letters, 1987. **59**(3): p. 292.

36. Mori, W.B., et al., *Raman forward scattering of short-pulse high-intensity lasers.* Physical Review Letters, 1994. **72**(10): p. 1482.

Chapter 4 Electron Acceleration in Laser-cone Interactions

4.1 Introduction

High energy electrons can also be generated in laser solid density plasma interactions. These so-called hot or fast or super-thermal electrons whose energies are much higher than the bulk plasma temperature are produced mainly by a variety of collisionless mechanisms such as resonance absorption [1], vacuum heating [2], and relativistic $\mathbf{J}\times\mathbf{B}$ heating [3]. These collisionless mechanisms compete with each other depending upon the conditions of laser light (intensity, duration, contrast ratio, etc.) as well as plasma target (material, geometry, scale length, etc.), and produce hot electrons with different angular distributions. The resonance absorption and vacuum heating mechanisms are expected to produce hot electrons in the direction of the density gradient ∇n_e both forward and backward. The $\mathbf{J}\times\mathbf{B}$ heating mechanism produces hot electrons in the direction of laser light propagation $\mathbf{k}_L$.

Besides hot electrons produced by these basic collionless heating mechanisms, a single narrow self-focused current jet of energetic electrons into the low density corona normal to the target was first observed under the oblique incidence of a p-polarized laser beam in PIC and Vlasov simulations [4]. Furthermore, the energetic electron jets in the laser specular reflection direction and the collimation effect of self-induced quasistatic magnetic field have been investigated by 2D PIC simulations [5]. However, in the case of sharp plasma density gradient and large laser incident angle, electron jet disappears and the charge current is confined on the surface of target. The surface current confinement is important for cone fast ignition scheme and was explained by a simple model of the transition to a steady state of an open system [6]. Moreover, electron bunches of attosecond duration generated in the interactions of P-polarized ultraintense laser pulses with sharp boundaries of overdense plasma were reported and demonstrated by PIC simulations [7]. The generation of these attosecond electron bunches is interpreted that a group of counterstream electrons escape from the bulk plasma and inherit a peaked electron density distribution. In Section 4.2, a new mechanism responsible for the generation of charge current or electron bunches along the surface of overdense plasma is proposed, where the obliquely incident intense laser light interacts with the surface electron ripple.

Moreover, the transfer of energy from the laser pulse to hot electrons is one of

the critical issues for the fast ignition of inertial confinement fusion. As we mentioned in the Chapter 1, the reentrant cone target was proposed for fast ignition to avoid the laser propagation loss and reflection by high-density plasma [8]. Meanwhile, cone target can focus the laser energy and guide high energy electrons to the cone tip [9], which results in higher energy coupling from the laser to hot electrons. In interaction of intense laser with cone plasma target, electron bunches generated by the mechanism described in Section 4.2 can be guided to the cone tip and accelerated once again by the focused laser light through **J**×**B** and wavebreaking mechanisms near the tip of the cone. In Section 4.3, this re-acceleration effect is demonstrated by 2D PIC simulations.

Furthermore, in cone target fast ignition, cone target is surrounded by a corona plasma generated by the implosion of a fuel capsule. The radiation hydro code PINOCO [10] shows that corona plasma density is well above the critical density. In this case, electrons accelerated by the laser field can escape freely from cone side to the surrounding corona plasma, resulting in the decrease of the energy flux through the cone tip. Nakamura *et al*. [11] have suggested a double-layer cone target to prevent the electrons from escaping aside. Their results show that double-layer cone target takes the advantages of confining the electrons in hundreds of femtoseconds with an immobile ion background. However, the plasma expansion can be very significant for picoseconds time scale simulation since the ions can be effectively heated, especially for the cone target cases. The sheath field inside the gap can be reduced to a very low level after a picosecond. Therefore, there are several points still need to be clarified. In Section 4.4, 2D PIC simulation is used for the investigation aiming at increasing the number of high energy electrons deposited to the compressed pellet by using double-layer cone target.

4.2 Generation of surface hot electrons by obliquely incident laser light

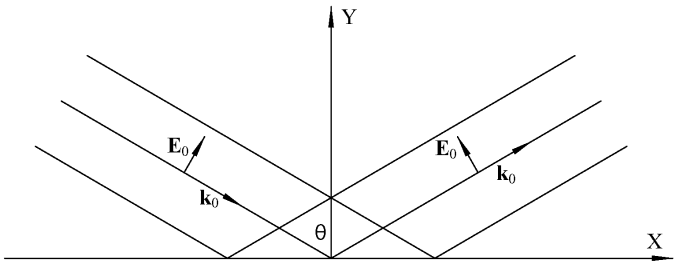

Fig. 4.1 Incidence of a laser beam on an overdense plasma surface

Consider a P-polarized laser pulse of finite width is obliquely incident on the surface of a perfect conductor or an overdense plasma, as shown in Fig. 4.1. The incident electric field is

$$\mathbf{E}_{inc}(x,y) = E_0 \cos(xk_0 \sin\theta - yk_0 \cos\theta - \omega_0 t)(\cos\theta\vec{i} + \sin\theta\vec{j}) \tag{4.1}$$

Here E_0 is the amplitude, ω_0 and k_0 are the frequency and wave number of incident laser light. The incident angle is θ, $\vec{i}$ and $\vec{j}$ are the unit vectors in X and Y directions. Then the electric field of reflected laser light is

$$\mathbf{E}_{ref}(x,y) = E_0 \cos(xk_0 \sin\theta + yk_0 \cos\theta - \omega_0 t)(-\cos\theta\vec{i} + \sin\theta\vec{j}) \tag{4.2}$$

In the triangle region, superposition of the incident laser light and the reflected laser light makes net electric field $\mathbf{E}(x, y) = \mathbf{E}_{inc}(x, y) + \mathbf{E}_{ref}(x, y)$, whose components in X and Y directions are

$$E_x(x,y) = -2E_0 \cos\theta \sin(xk_0 \sin\theta - \omega_0 t)\sin(yk_0 \cos\theta) \tag{4.3}$$

$$E_y(x,y) = 2E_0 \sin\theta \cos(xk_0 \sin\theta - \omega_0 t)\cos(yk_0 \cos\theta) \tag{4.4}$$

From Eq. (4.3), we can see, on the surface where $y = 0$, $E_x(x,y) \propto \sin(yk_0 \cos\theta) = 0$, electric field only has component normal to the surface with amplitude of $2E_0\sin\theta$. This normal electric field plays the key role in the vacuum heating mechanism. In the model of vacuum heating, the normal electric field drags electrons into vacuum and then pulls them back into the plasma. This pulling and pushing effect by the electric field will generate electron density ripples (convex and concave) on the plasma surface when the laser light is injected obliquely. The amplitude of electron density ripples is proportional to the laser intensity. When the laser intensity is high enough, the amplitude of the plasma surface ripple can be as high as the scale of laser wavelength. As shown in Eq. (4.4), in the vacuum region above the surface where $y>0$, electric field has component parallel to the plasma surface with amplitude of $2E_0\cos\theta$. This component can impact on the projected ripples and drag them forward along the plasma surface.

Then, we use 2D PIC simulation to demonstrate the effect described above. The target is 30° oblique to the X-axis and consisted of fully ionized plasma with the density of $10n_c$. A P-polarized laser is incident into the simulation box from left to right along the X-axis. Transversely, the laser pulse is Gaussian with $1.2\lambda_0$ (FWHM),

and it rises up longitudinally in $1\tau_0$ and then maintains the peak intensity semi-infinitely. The peak normalized laser vector potentials, $a_0=eA/m_e\omega_0c^2$.

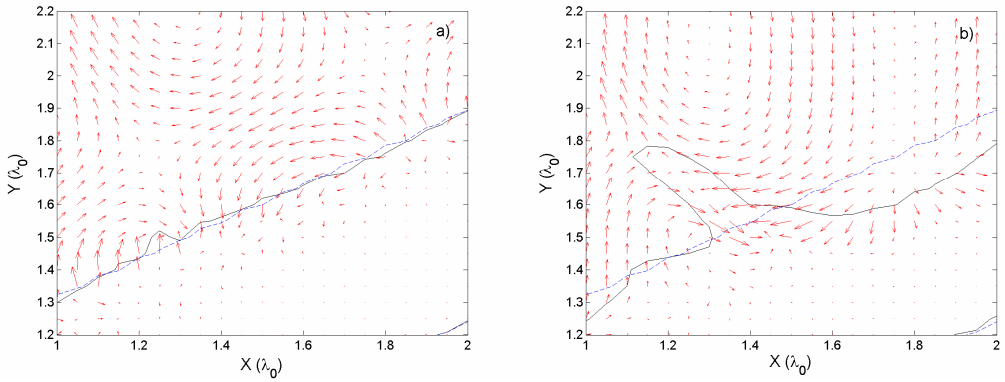

Fig. 4.2 Contour of critical electron density of plasma at t=0 (black) and t=3τ_0 (blue), and distribution of electric field (red arrow) for a) a_0=0.2 and b) a_0=5.0.

In Fig. 4.2, red arrows display the spatial distribution of electric field vectors near the surface of plasma target for a_0 = 0.2 and 5.0. For low intensity laser, as Fig. 4.2 a) shows, the electron density is almost kept the same as initial one. But for high intensity laser, as Fig. 4.2 b) shows, the generation of density ripples is clearly observed. Where the electric field is positive, electrons are pushed back, so the plasma surface is concave. Where electric field is negative, electrons are dragged out, so the plasma surface is convex and the ripple is formed. The ripple extends into the vacuum about tens of percent of λ_0, and the reflection of incident laser is modified locally. As shown in Fig. 4.2 b), at the foreside of the ripple, the parallel component of the electric field is very strong. And this electric field component can drag electrons forward.

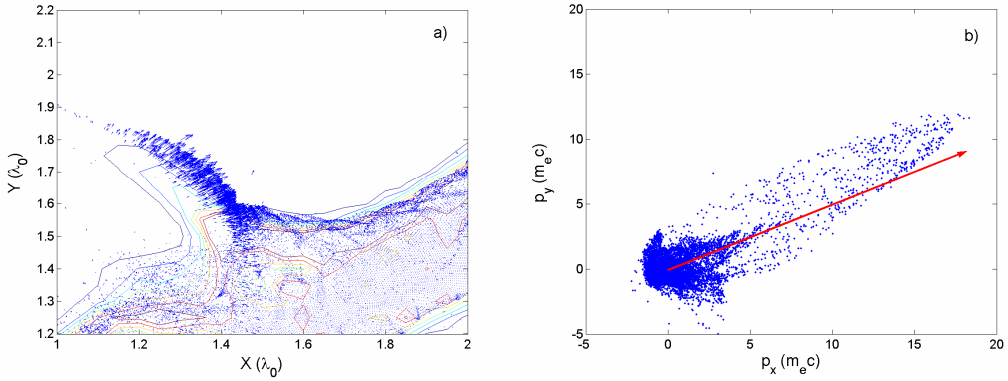

Fig. 4.3 a) Contours of electron density and vector distribution of electrons; b) Distribution of electrons in the momentum phase space, at t=3τ_0 for P-polarization and a_0=5.0.

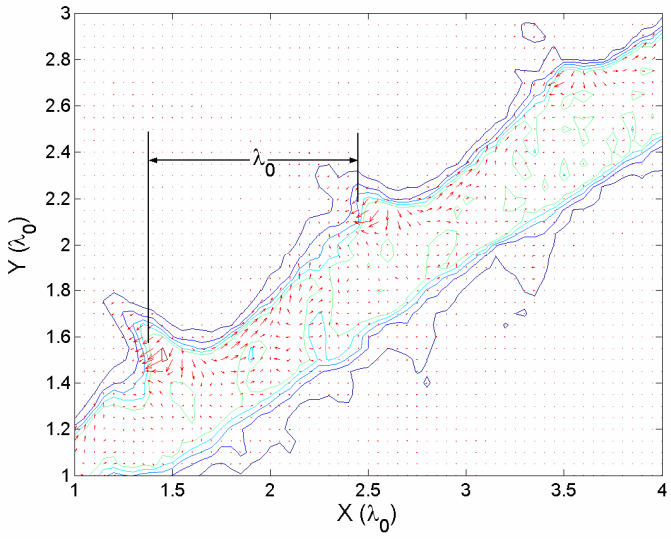

Fig. 4.4 Contour of electron density and vector distribution of charge current at $t=6\tau_0$ for P-polarization and a_0=5.0.

Distribution of electrons velocity vectors for $a_0 = 5.0$ at $t = 3\tau_0$ is shown in Fig. 4.3 a). A fraction of electrons located at the foreside of the ripple have velocities much higher than those of thermal electrons and parallel to the plasma surface, which is consistent with the local distribution of electric field vector as shown in Fig. 4.2 b). The distribution of electrons in momentum phase space p_x vs p_y is shown in Fig. 4.3 b). The red arrow line points to the direction of 30°. It is illustrated that most of hot electrons have velocity parallel to the target surface. And we believe that the parallel electric field component accelerated these hot electrons.

Fig. 4.4 shows the vector distribution of charge current and contour of electron density in a large area. The most outside contour line represents the critical density n_c. We can see electron bunches with density around initial electron density n_0 are flowing along the plasma surface. The spacing between them is about $1\lambda_0$. But their width is much shorter than λ_0. In the region between every two neighboring bunches, there is return current which in the direction opposite to electron bunches. The forward surface current and backward return current are responsible for the generation of quasistatic magnetic field which can maintain the surface electron flow [9].

The density ripple is generated only for high-intensity, obliquely incident and P-polarized laser light and critical for the generation of this surface electron bunches. To confirm the above effect existing only for P-polarized laser light pulse, a case of S-polarization is simulated. It is shown in Fig. 4.5 a) that, for S-polarization, no high amplitude electron density ripples are formed and there are no electros accelerated

along the target surface. From the distribution of electrons in momentum phase space, Fig. 4.5 b), velocity of electrons is much lower than the P-polarization case. And we can see, energetic electrons are accelerated forward with an angular spread according to the **J**×**B** mechanism. At such high laser intensities, ponderomotive force is assumed to be independent on polarizations. So, it is confirmed that the effective injection of hot electrons is due to the parallel component of the net electric field.

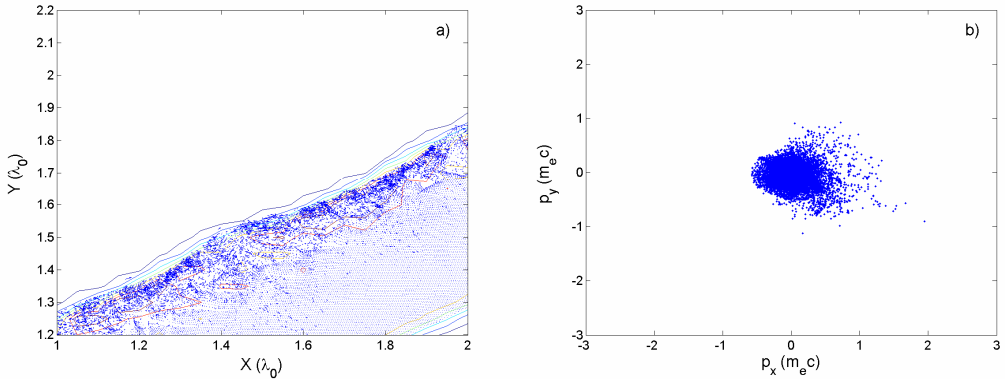

Fig. 4.5 a) Contours of electron density and vector distribution of electrons; b) Distribution of electrons in the momentum phase space, at t=3τ_0 for S-polarization and a_0=5.0.

4.3 Re-acceleration of surface electrons in laser-cone interaction

2D PIC simulations are used to demonstrate the re-acceleration of surface electron bunches in intense laser-cone interactions. The simulation box is $60\lambda_0 \times 40\lambda_0$ with cell size of $0.05\lambda_0$. The cone target has open angle of 30° and consists of fully ionized plasma with density of $10n_c$. The initial temperatures of electrons and ions are both 1.0 keV. A P-polarized Gaussian laser beam with a focal spot of $6\lambda_0$ (FWHM) is incident to the simulation box along the X axis from left to right. The laser beam rises up in $5\tau_0$ with a sinusoidal profile, after which it maintains its peak normalized vector potential a_0 = 5.0.

In Fig. 4.6 a), solid black line represents the initial critical density of cone plasma n_c; color image shows the spatial distribution of forward charge current J_x at t = 35τ_0. We can see electron bunches are flowing forward on the surface of cone plasma. The phase difference of electron bunches on the surfaces of upper and bottom sides is $\lambda_0/2$ which is consistent with the phase difference of electromagnetic field of incident laser light. Fig. 4.6 b) shows the distribution of electrons in momentum phase space at the same time and illustrates that these surface electron bunches have much higher energy

than thermal plasma electrons.

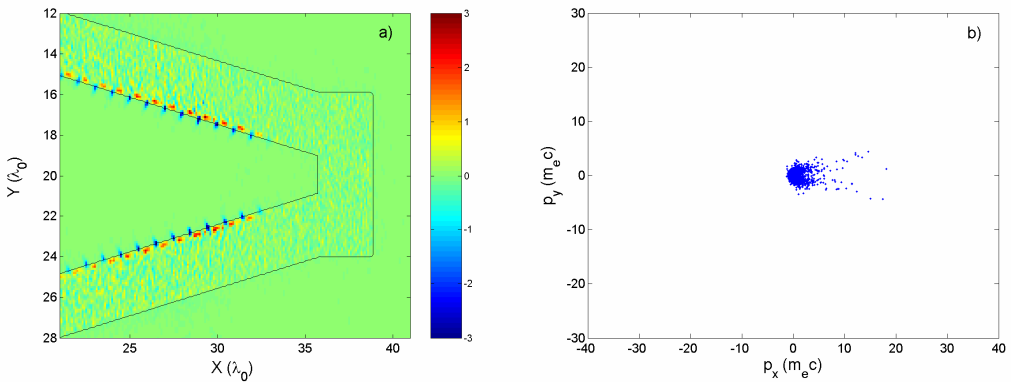

Fig. 4.6 a) Spatial distribution of initial critical density n_c and forward charge current J_x; b) Distribution of electrons in the momentum phase space at t = 35τ_0.

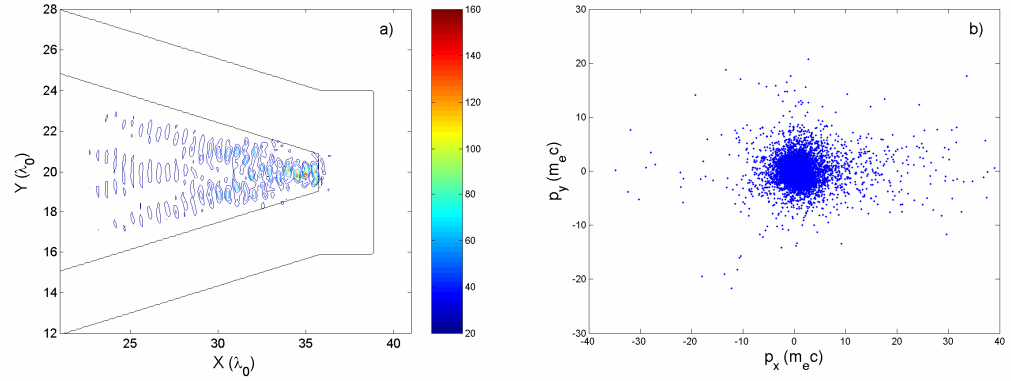

Fig. 4.7 a) Spatial distribution of initial critical density n_c and energy density of laser light; b) Distribution of electrons in the momentum phase space at t = 50τ_0.

When wave front reaches the cone tip, the focused laser light interacts with the cone tip strongly. The light pressure at the tipis increased significantly due to the focusing effect of cone target. Fig. 4.7 a) illustrates the focusing of laser light by cone target. Initial energy density of incident laser light is normalized as $W_0 = a_0^2 = 25$. After the focusing at t = 50τ_0, it is increased to 160, about 6.4 times higher. Surface electron bunches flow to the cone tip continuously and are re-accelerated by the enhanced laser light. Fig. 4.7 b) shows the distribution of electrons in momentum phase space at t = 50τ_0 after the re-acceleration happens. We can see most of high energy electrons are forward and in an angle equal to the open angle of cone target. The maximum energy of forward accelerated hot electrons is around 20 MeV.

To confirm that these electrons are generated by the re-acceleration of surface electron bunches, the case of S-polarized incident laser light is simulated. For

S-polarization, hot electrons mainly originate from the cone tip interacting with the focused laser light since no injection of surface bunches occurs in this case. Fig. 4.8 a) shows the distribution of electrons in momentum phase space at $t = 50\tau_0$ for S-polarization. Fig. 4.8 b) illustrates the energy spectra of electrons for P- and S-polarizations. We can see, compared with S-polarization, more electrons are accelerated forward and to higher energies for P-polarization. From the above discussion, it can be confirmed that these hotter forward electrons are owed to the re-acceleration of surface electron bunches in the P-polarized laser-cone interactions.

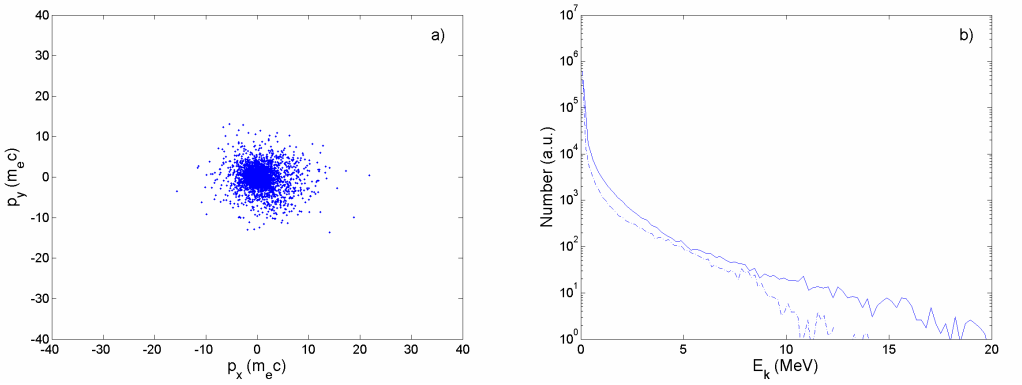

Fig. 4.8 a) Distribution of electrons in the momentum phase space at $t = 50\tau_0$ for S-polarization; b) Energy spectrum of electrons at $t = 50\tau_0$ for P-polarization (solid line) and S-polarization (dashed line)

4.4 Confinement of hot electrons via double-layer cone target

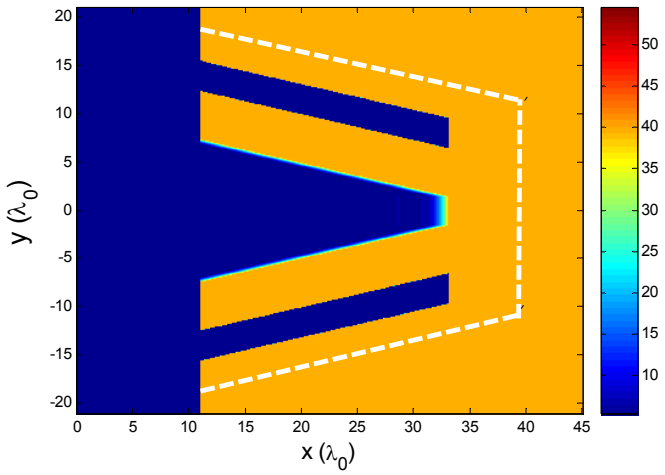

Fig. 4.9 Schematic of the double cone target.

In this Section, 2D PIC simulation is used to investigate the confinement of hot

electrons via double-layer cone target. Fig. 4.9 shows the sketch of the geometry of the simulations. In the double-layer cone target, inner cone wing is isolated from the background plasma (corona plasma) due to the vacuum gap. Here, the width of the inner cone wing is $5\lambda_0$ and the width of the gap is $3\lambda_0$. The plasma density is $40n_c$, the initial electron temperature is set to be 1keV and the ion temperature is set to 0.1 keV. The laser pulse irradiates the target from the left boundary whose intensity is $10^{19} W/cm^2$. The laser field is P-polarized. The intensity profile is Gaussian in the y-direction with a spot size of $5.0\mu m$ (FWHM). The laser rises up in $20\tau_0$, after which the laser amplitude is kept constant.

The target geometry is very close to the simulations that were performed in Ref. [11], but our work was performed with movable ions and under much longer time scales and larger space scales. In picosecond time scale, we found that the plasma temperatures in the inner cone area were heated up much faster than that of the single cone case, resulting in a significant plasma expansion into the vacuum gap inside the cone wing. This plasma expansion can decrease the sheath field at the rear side of the inner cone.

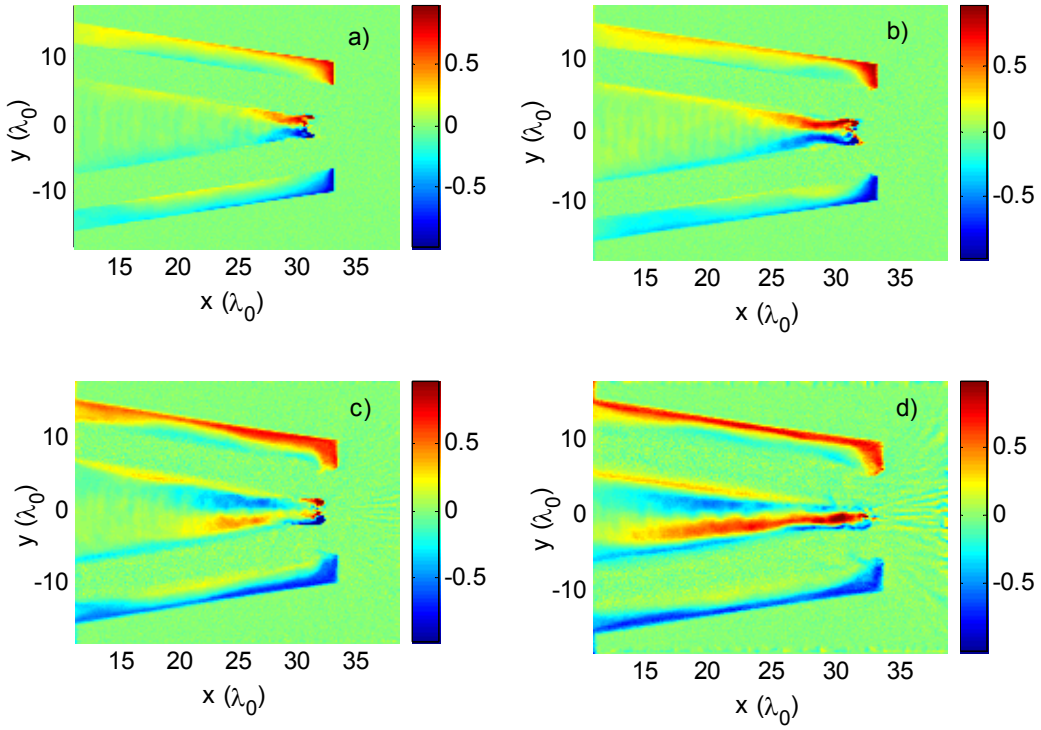

Figure 4.10 Quasistatic magnetic fields at four different times: a) $t = 100\tau_0$, b) $150\tau_0$, c) $333\tau_0$, and d) $450\tau_0$.

Figure 4.10 shows the quasistatic magnetic fields at four different times: a) t = $100\tau_0$, b) $150\tau_0$, c) $333\tau_0$, and d) $450\tau_0$. Note that the magnetic fields inside the gap first appear at the region close to the cone tip since at early time the magnetic fields are mainly generated by the return current from the cone tip. As time goes on, the magnetic fields grow to the whole gap area. The quasistatic electric field peaks at time $t = 75\tau_0$, and eventually decreases to very low level after time $t = 180\tau_0$. In comparison, the quasistatic magnetic field does not decrease with time after it grows up at time t = $100\tau_0$. Since the average electron cyclotron radius is $R = m_e v_{th} c / eB_s$, here v_{th} is the thermal velocity of hot electrons. So even for MeV hot electrons, the electron cyclotron radius is only $R \sim 0.15\lambda_0$ under such a large quasistatic magnetic field. Therefore, the electrons escaping into the vacuum gap can be effectively turned back by the magnetic fields.

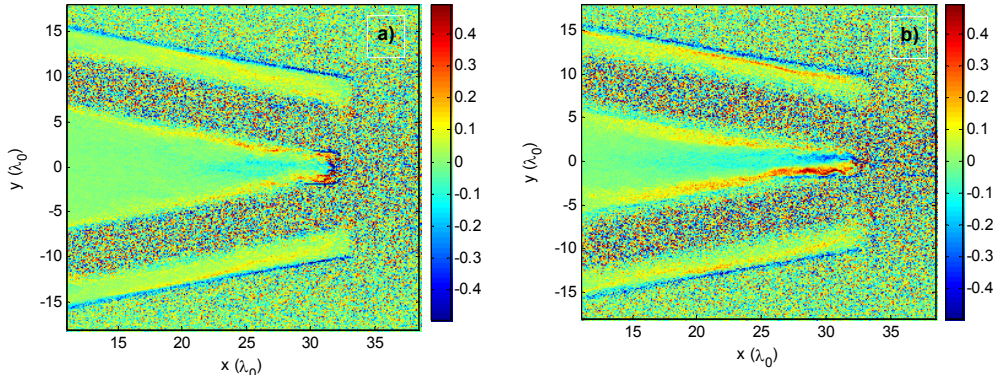

Figure 4.11 Time averaged current J_x at (a) $333\tau_0$, and (b) $450\tau_0$.

Figure 4.11 shows the time averaged longitudinal current J_x at t = $333\tau_0$ and $450\tau_0$. We notice that there are two oppositely directed currents inside the gap. The positive one is mainly produced by the return electrons coming from the cone tip; while the negative one is a surface current moving along inner surface of the outer cone. The collaboration of these two currents can therefore give rise a large quasistatic magnetic field inside the gap.

Table 4.1 Fraction of escaped energetic electrons at different boundaries for double-layer cone target and single cone target.

	right %	down %	up %	left %
Gap	31.4	12.5	11.4	0.41
No Gap	38.4	4.5	4.4	0.41

The fraction of escaped energetic electrons, defined as the ratio of the escaped electrons kinetic energy from each boundary to the total input energy of the laser energy, for the single cone target case and double-layer cone case with a three micrometers gap, is plotted in Table 4.1. Here, the escaped high energy electrons are collected by the collectors placed beside the boundaries. In the single cone target case, only 56.7% of the total energy the escaped energetic electrons can accelerate to the cone tip (right boundary). When using a double-layer cone target, this fraction can be as high as 81.3%.

4.5 Conclusion

The injection of hot electrons induced directly by the oblique incident laser on high gradient plasma surface is presented and investigated by theoretical analysis and 2D PIC simulations. It is demonstrated that high electric normal component can drag electrons into the vacuum to form the convex on the plasma surface. The convex affects the reflection of laser light so that the parallel component of electric field located at the foreside of the convex can pull it forward. This effect can generate high current along the plasma surface.

In the cone target scheme of fast ignition, 2D PIC simulation results show these energetic electron bunches are confined to the cone tip on the surface of cone wall and re-accelerated by the focused laser light at the cone tip. This re-acceleration effect has advantages of enhancement of energy of hot electrons and coupling from laser to hot electrons.

Moreover, it is shown that the energy flux through the cone tip using the double-layer cone target is much larger and more focusing than the single cone target. At the beginning of interaction, the sheath fields at the rear of inner cone wing are strong enough to confine the high energy electrons. But the sheath fields decrease to very low level after several hundreds of femtoseconds because of plasma expansion. In contrast, the quasistatic magnetic fields, which are generated by the surface current along the inner surface of the outer cone, can be still as high as 100MG even at a long time, which are the real reason for confining the high energy electrons.

Reference

1. Ebrahim, N.A., et al., *Hot Electron Generation by the Two-Plasmon Decay Instability in the Laser-Plasma Interaction at 10.6 mum.* Physical Review Letters, 1980. **45**(14): p. 1179.

2. Brunel, F., *Not-so-resonant, resonant absorption.* Physical Review Letters, 1987. **59**(1): p. 52.

3. Kruer, W.L. and K. Estabrook, *J x B heating by very intense laser light.* Physics of Fluids, 1985. **28**(1): p. 430-432.

4. Ruhl, H., et al., *Collimated Electron Jets by Intense Laser-Beam-Plasma Surface Interaction under Oblique Incidence.* Physical Review Letters, 1999. **82**(4): p. 743.

5. Sentoku, Y., et al., *Plasma jet formation and magnetic-field generation in the intense laser plasma under oblique incidence.* Physics of Plasmas, 1999. **6**(7): p. 2855-2861.

6. Nakamura, T., et al., *Surface-Magnetic-Field and Fast-Electron Current-Layer Formation by Ultraintense Laser Irradiation.* Physical Review Letters, 2004. **93**(26): p. 265002.

7. Naumova, N., et al., *Attosecond Electron Bunches.* Physical Review Letters, 2004. **93**(19): p. 195003.

8. Kodama, R., et al., *Fast heating of ultrahigh-density plasma as a step towards laser fusion ignition.* Nature, 2001. **412**(6849): p. 798-802.

9. Sentoku, Y., et al., *Laser light and hot electron micro focusing using a conical target.* Physics of Plasmas, 2004. **11**(6): p. 3083-3087.

10. Nagatomo, H., et al. *Computational study of implosion physics and target design for the fast ignition experiment FIREX-I.* in *Journal De Physique. IV : JP*. 2006. Biarritz.

11. Nakamura, T., et al., *Optimization of cone target geometry for fast ignition.* Physics of Plasmas, 2007. **14**(10): p. 103105-7.

Chapter 5 An Application of Hot Electrons from Laser Plasma Accelerator - Proton Acceleration in Laser cone Interactions

5.1 Introduction

One of the wonderful applications of hot electrons from laser plasma accelerator is the generation of high energy ion beams. With current CPA technology ions are not easy to be accelerated to high energy directly by the laser field because of their much higher mass compared to that of electrons. However, in plasmas, intense laser lights interact with electrons and push them around; the electric fields via charge separation between electrons and ions are so high that the ions can be accelerated to high energies.

The emission of energetic ions in laser-plasma interactions for nanosecond time scale was first observed in experiment in 1960's [1]. Over the last fifteen years, a number of experiments on the generation of forward multi-MeV ions for CPA laser lights at intensities over 10^{18} W/cm^2 were reported and interpreted with remarkably different mechanisms for origin and acceleration. One mechanism interpreted that high-energy proton beams were originated and accelerated at the front surface of target where incident laser pulse interacted with overdense plasma [2, 3] which was supported by the ring structure emission of protons; the other mechanism argued that forward high-energy proton beams originated and were accelerated at the rear surface of the target, which was supported by the evidence that protons were emitted perpendicular to the rear surface of the wedge-shaped targets [4].

The full discussion of the model proposed in Ref. [4] was presented and demonstrated by PIC simulation [5]. When intense laser light is incident on a planar plasma, hot electrons are generated at the interaction surface. Hot electrons can propagate through the target and produce a strong electrostatic field normal to the rear surface of target due to charge separation, which results in the acceleration of ionized protons in a contaminant. This is termed the target normal sheath acceleration (TNSA) mechanism [5]. From Poisson's equation and Boltzmann statistics for electrons, the accelerating electric fields acting on the ions was estimated as $E=T_h/e\max(L_n, \lambda_D)$, here L_n is the density scale length of hot electrons, and λ_D is the Debye length.

The typical energy spectrum of forward accelerated protons or ions has a quasithermal distribution with a cutoff at a maximum energy. The mean energy of

protons is much smaller than the maximum cutoff energy, namely, their spectrum has almost 100% spread. However, applications of high-energy ions require high-quality ion beams with small energy spread. In order to obtain quasi-monoenergetic proton beams, a scheme using microstructured double-layer target was proposed and demonstrated by 3D PIC simulations [6]. The first layer at the front side of the target consisted of high-Z atoms. The second layer was a low-Z material ultrathin longitudinally and small transversely coated on the rear side of the first layer. With the parameters of PIC simulations in Ref. [6], quasi-monoenergetic protons has energy spread $\Delta E/E_{max}<5\%$ with $E_{max}\sim65$ MeV. Experiments based on the scheme in Ref. [6] was carried out by H. Schwoerer *et al*. [7]. The high intensity laser pulse had duration of 80 fs and peak intensity at 3.0×10^{19} W/cm^2. The target was 5 μm thin titanium film coated with a 0.5 μm PMMA dot with 20×20 μm^2. Energy spectrum of the observed proton beams exhibited a narrow band of $\Delta E/E_{max}\sim25\%$ with $E_{max}\sim1.5$ MeV.

Critical for the acceleration of monoenergetic protons is the absorption efficiency of laser energy to hot electrons, since protons are accelerated by the electric fields induced by the charge separation of hot electrons and background ions. A target design of the re-entrant cone geometry [8] for fast ignition has attracted considerable interest. PIC simulations proved the cone target can increase the energy coupling from the laser pulse to electrons effectively [9]. A cone target is also proposed to enhance the generation of protons in simulation [10] and experiment [11]. But in these two references, the energy spreads of accelerated protons are almost 100% and it is not clear that if the cone target will damage the monochromaticity of protons.

In this chapter, a new scheme to increase the energy of quasi-monoenergetic protons is proposed. In this scheme, a cone-shaped target of high-Z material is used to interact with an ultrashort intense laser light for improving the generation and confinement of hot electrons. The rear surface of this target is coated with an extra ultrathin proton layer with relatively low density to act as the source of proton for the acceleration. Due to the proton acceleration mechanisms, protons are accelerated by the sheath field produced by hot electrons on the boundary between the high-Z substrate and the proton layer. As a result, the higher energy and density of hot electrons in the cone target increase the proton energy.

5.2 PIC simulations

Two-dimensional PIC simulations were performed to investigate the above

process. The scales of the simulation box are $X\times Y=60\lambda_0\times 40\lambda_0$ with a cell size of $\Delta X=\Delta Y=0.05\lambda_0$, where λ_0 is the wavelength of the incident laser light. A linearly polarized Gaussian laser beam with a focal spot of $6\lambda_0$ (FWHM) is incident to the simulation box along the X axis from left to right. The laser beam rises up in $5\tau_0$ with a sinusoidal profile, after which it maintains its peak intensity for $20\tau_0$, and then falls to zero in another $5\tau_0$, where τ_0 is the laser period. The peak normalized vector potential is $a_0=eA/m_e\omega_0c^2=5.0$, which corresponds to the peak incident intensity $I_0=3.5\times10^{19}$ W/cm^2.

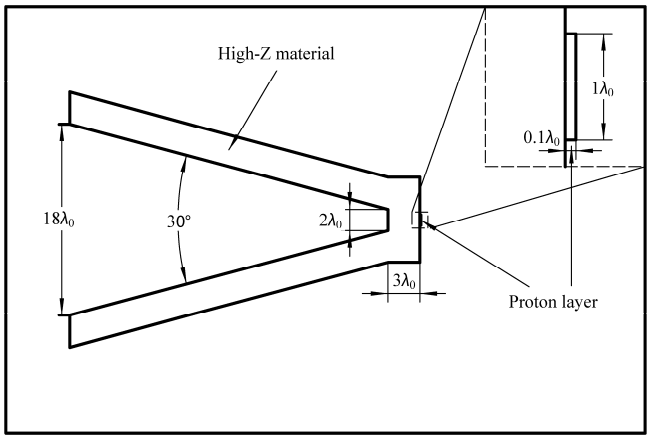

Fig. 5.1 Schematic of the cone-shaped substrate and the coated proton layer.

The geometry of the cone-shaped substrate and coated proton layer is shown in Fig. 5.1. The width of the cone wall is $3\lambda_0$, the open hatch and the tip are $18\lambda_0$ and $2\lambda_0$ wide, respectively, and the open angle is 30° which is the optimum angle for laser cone interactions [12]. The cone substrate consists of partially ionized plasma where the effective charge-to-mass ratio Z/A is assumed to be 1/10. The electron density of the target is 10 times the critical density (n_c), which is related to the frequency of the incident laser as $\omega_0^2=4\pi e^2 n_c/m_e$. The initial electron and ion temperatures are both 1.0 keV. At the rear surface of the cone substrate, there is a proton layer with density of $1n_c$, which is shown in the dashed square in Fig. 5.1.

To demonstrate the advantage of cone target for laser proton acceleration, a scheme with film substrate is simulated. For the film target, the high-Z layer is $18\lambda_0$ wide and $3\lambda_0$ thick. The proton layers for cone substrate and film one are both $1\lambda_0$ wide and $0.1\lambda_0$ thick. Because the protons on the target's rear surface are accelerated directly by the sheath field due to the TNSA mechanism, first the spatial distribution of normalized E_x which is averaged over one laser period from $t=60\tau_0$, namely the

electrostatic sheath, for both targets are plotted in Fig. 5.2. Strong electrostatic fields around 6×10^{12} V/m are built up at both front and rear sides of the target independent on its geometry. At the front surface of the target, electric field turns from negative to positive within one laser wavelength. The negative electrostatic field is induced by the charge separation of expanding electrons and drags a faction of ions backward. The positive one is induced from forward hot electrons generated by the ponderomotive force of incident laser light and pushes a fraction of ions forward, which is supported by the evidence that the transverse size of the positive electric field is of the scale of the focal spot of incident laser pulse as shown in Fig. 5.2 b).

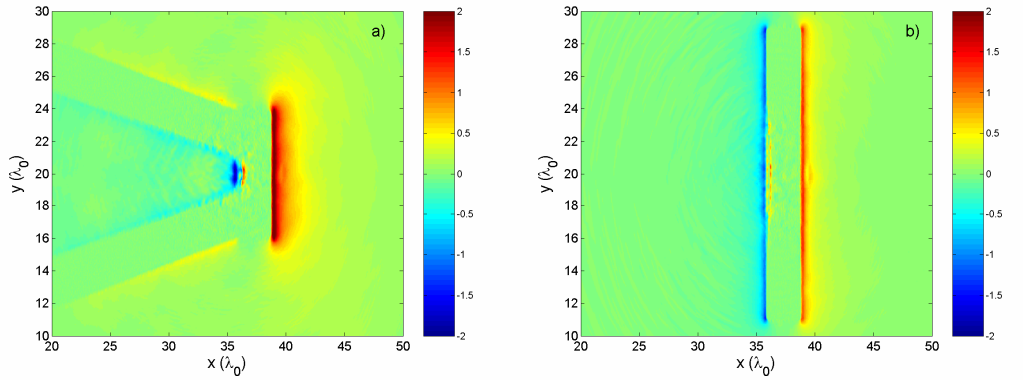

Fig. 5.2 Spatial distribution of normalized E_x averaged over one laser period from t=60τ_0 for a) cone target and b) film target.

On the rear surface of the target, we can see, only positive electric field is set up due to the hot electrons propagating from the laser plasma interface to the rear surface of target. This is consistent with the model of TNSA [5]. Evolution of the on-axis distributions of sheath fields for cone and film targets is plotted in Fig. 5.3. We can see that at all times the amplitude and the range of the electric field on the rear surface of the cone target (solid line) is much higher than those for the film target (dashed line), as expected. The electrostatic field's higher and wider amplitude indicates higher acceleration for the cone target.

Enhancement of the sheath field is believed to result from the increase of hot electrons generated by the cone target. From the TNSA mechanism [5], the amplitude of the sheath field on the target's rear surface is proportional to the temperature of hot electrons (not thermal electrons). When an intense laser light interacts with the side wall of the cone target, electrons are confined on the surface to the tip by the self-induced surface magnetic field [9]. Meanwhile, the laser pulse is focused by the

conical surface, and its intensity can be increased by a few of times. The temperature of hot electrons is $T_h = 511[(1+0.73I\lambda^2)^{1/2}-1]$ keV due to the **J**×**B** mechanism predominant in this interaction. Thus, the temperature of hot electrons is increased significantly by the focused laser light, and so is the accelerating sheath field.

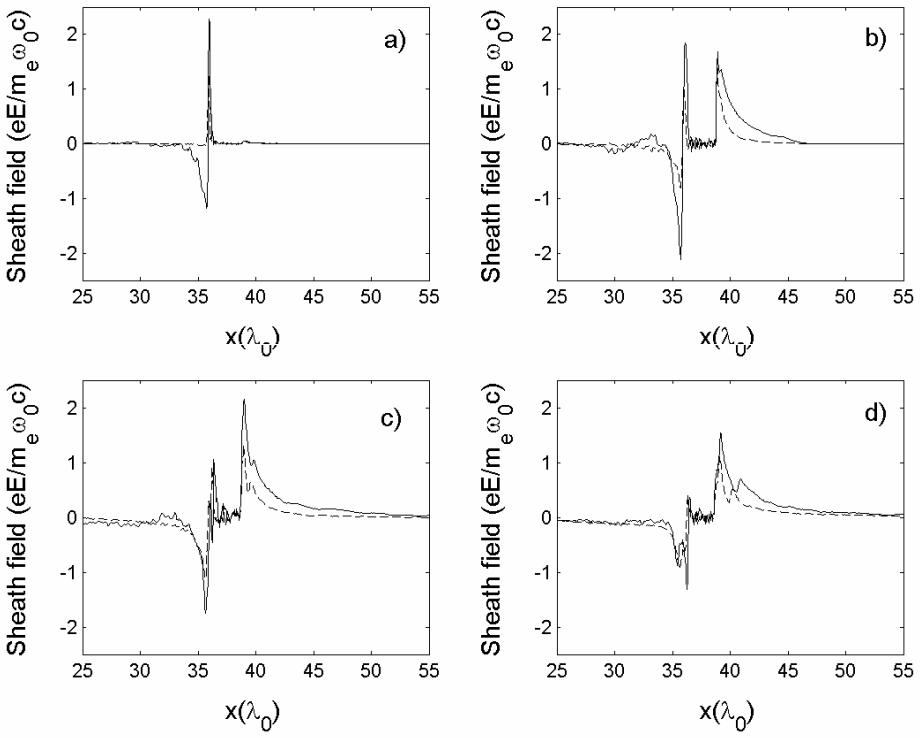

Fig. 5.3 On-axis distribution of sheath fields for cone target (solid line) and film target (dashed line) at a) t=40τ_0, b) 50τ_0, c) 60τ_0, d) 70τ_0.

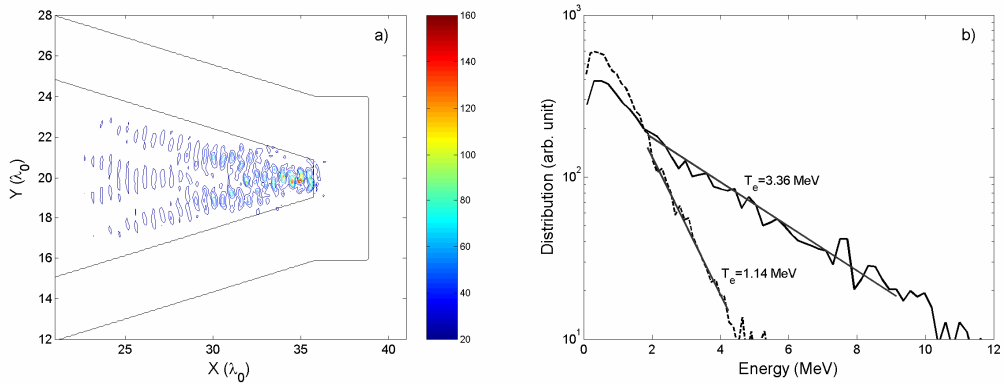

Fig. 5.4 a) spatial distribution of laser energy density at t=50τ_0 for cone target; b) spectra of electrons escaping from the rear surface of cone target (solid line) and film target (dashed line).

Fig. 5.4 a) shows the spatial distribution of laser energy density for cone target.

At the cone tip, laser energy density is increased about 6.4 times higher than the incident one. From the scaling law of **J**×**B** mechanism, the temperature of hot electrons should be increased 2.5 times higher. The energy spectra of hot electrons escaping from the targets' rear surface are plotted in Fig. 5.4 b). The electron temperature for film target is 1.14 MeV; for cone target it is 3.36 MeV, even higher than the expectation from the scaling law given above. This can be interpreted by the re-acceleration of surface hot electrons by the focused laser light at the cone tip discussed in Chapter 4. Therefore, higher hot-electron temperature of the cone target accounts for the higher sheath field at the target's rear surface, which is consistent with the results shown in Fig. 5.3. The energy-transfer ratios from the laser to the hot electrons are 1.9% and 0.7% for the cone target and film target, respectively.

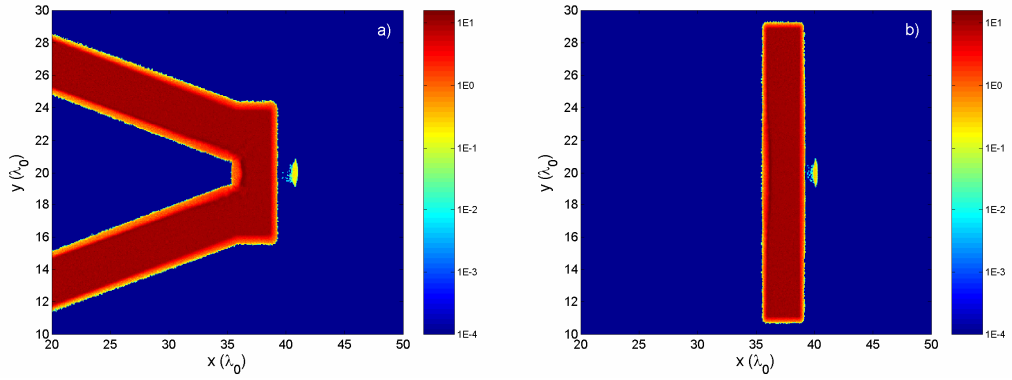

Fig. 5.5 Spatial distribution of ion density at t=70τ_0 for a) cone target and b) film target.

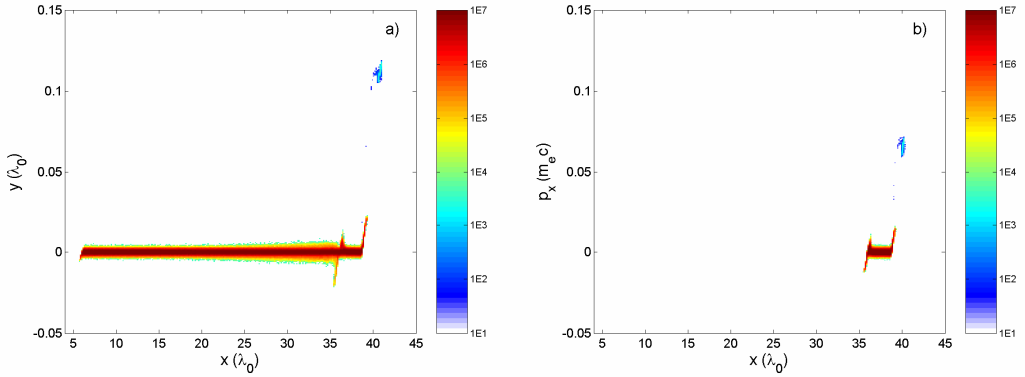

Fig. 5.6 Distribution of ions in phase space p_x *vs* x at t=70τ_0 for a) cone target and b) film target.

The above results demonstrate that the cone target can obtain higher temperature of hot electrons and the sheath field, which can accelerate protons on the rear surface, than the film target. Fig. 5.5 shows the 2D spatial distributions of ion density at t =

$70\tau_0$ for both target geometries. The proton layer coated on the rear surface of the substrate is accelerated to jet from the substrate as a whole due to the difference of mass of these two ion species. Fig. 5.6 shows the distribution of both heavy ions and protons in phase space p_x *vs* x at $t = 70\tau_0$ for cone target and film one. At the tip of cone target or front side of film target, a fraction of ions move backward and a fraction of ions move forward, which is consistent with the direction of sheath field shown in Fig. 5.2. Moreover, at the rear surface of the substrate, both heavy background ions and protons are accelerated forward by the sheath field. However, protons are accelerated to higher momentum because of their lighter mass. For cone target, momentums of protons are higher than those of film target according to the increase of sheath field discussed above.

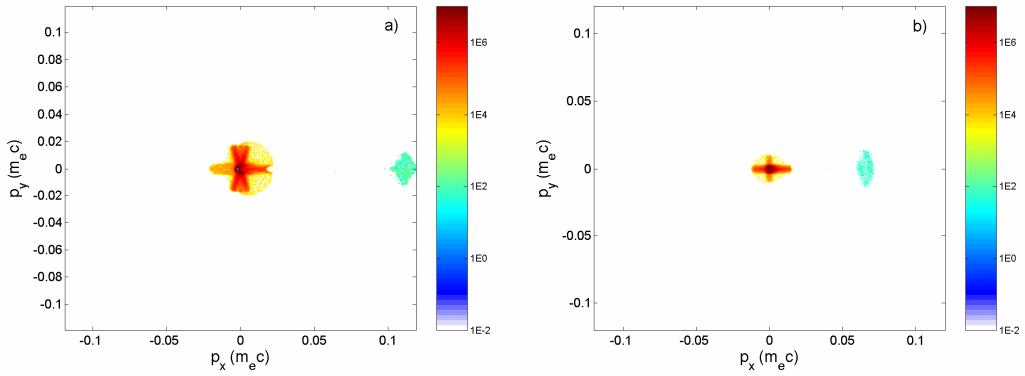

Fig. 5.7 Distribution of ions in phase space p_x *vs* p_y at t=$70\tau_0$ for a) cone target and b) film target.

From the distributions of ions in momentum phase space p_x *vs* p_y shown in Fig. 5.7, we can estimate the angular distribution of proton emission. For film substrate, protons are confined in a cone angle about 26°. For cone substrate, the cone angle is 12°, which means much better collimation than film target.

Fig. 5.8 shows the energy spectra of protons measured at t=70 τ_0, just after the incident laser light interacts with plasma. For the film target (dashed line), the peak proton energy is E_0=2.2 MeV, and the energy spread is $\Delta E_{FWHM}/E_0$=13.1%. For the cone target (solid line), the peak proton energy is E_0=5.9 MeV, 2.7 times higher than that of the film target, and the energy spread is $\Delta E_{FWHM}/E_0$=16.3%. The total energy transported from the laser to protons for the cone target is also about three times increased than the film target, which is consistent with the increase of hot electrons' temperature by cone target. It is confirmed that this cone substrate plus ultrathin

proton layer scheme can increase the energy of protons and the coupling from laser to protons by about three times while maintaining the protons' monochromaticity.

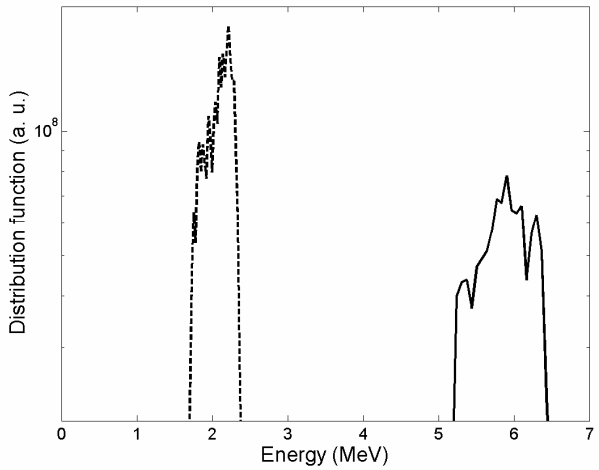

Fig. 5.8 Energy spectra of protons at t=70τ_0 for cone target (solid line) and film target (dashed line).

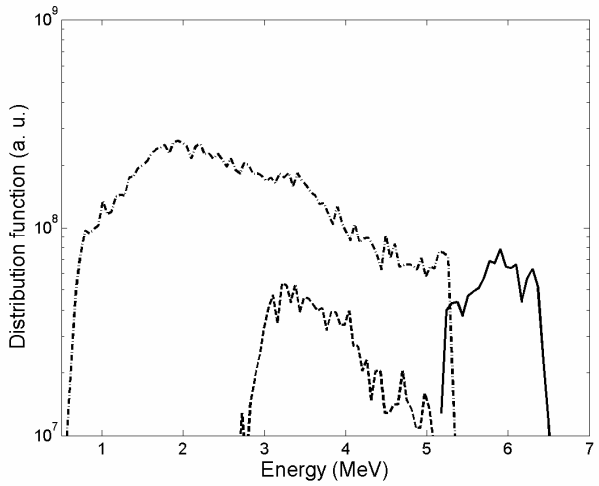

Fig. 5.9 Energy spectra of protons at t=70τ_0 for proton layer of $0.1\lambda_0\times1\lambda_0$ (solid line), $1.0\lambda_0\times0.1\lambda_0$ (dashed line), and $1.0\lambda_0\times1.0\lambda_0$ (dash-dot line).

The microstructured proton layer is the key for the generation of monoenergetic proton beams. Cases with different sizes of proton layer are simulated to check the effect of proton layer size to the monochromaticity of high energy proton beams. Besides the size in the above discussion, two more cases are simulated. One is $1.0\lambda_0\times0.1\lambda_0$ (thick×wide); the other is $1.0\lambda_0\times1.0\lambda_0$. Other parameters are the same as in Fig. 5.2 a). Energy spectra of protons of all three cases are plotted in Fig. 5.9. We can see, in the case of thinnest size, protons have maximum energy and best

monochromaticity. For larger size longitudinally even smaller in transverse direction, energy and monochromaticity of protons are both reduced. In the case of $1.0\lambda_0 \times 1.0\lambda_0$ size, protons' energy is reduced more and spreads almost 100%. This can be explained by the difference of field extend longitudinally and transversely. From the spatial distribution of electrostatic field in Fig. 5.3, we can see it is much sharper in longitudinal direction than in transverse direction. Only ultrathin proton layer can experience the same sheath field while being accelerated.

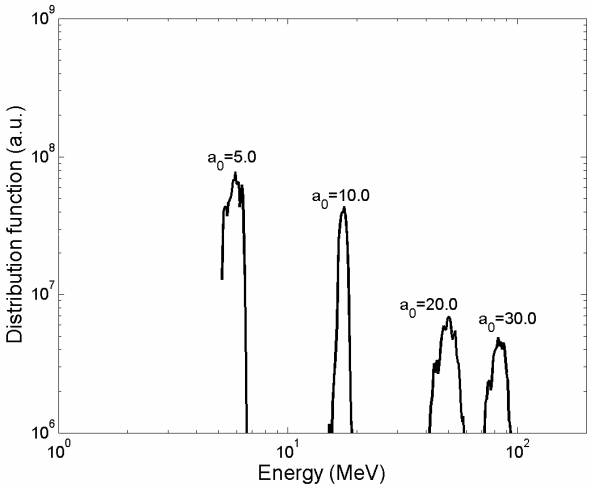

Fig. 5.10 Energy spectra of protons at $t=70\tau_0$ for a_0=5.0, 10.0, 20.0 and 30.0

Fig. 5.10 shows the energy spectra of protons *vs* laser intensities. Energy of proton beam is proportional to the normalized laser vector potential, which is consistent with TNSA mechanism and scaling law of **J**×**B** mechanism. When $a_0 = 30$, proton beam's energy can be as high as 83 MeV. If 3D effect of the laser focusing from cone target is taken into account, the energy can be high to around 100 MeV. The current PW laser facility has intensity over 1.0×10^{21} W/cm^2 and duration about 500 fs which is longer than that in my simulations and should be advantageous for proton acceleration. If the scheme discussed in this chapter is carried out under such laser pulse condition, 200 MeV monoenergetic proton beams which are appropriate for cancer therapy may be achieved.

5.3 Conclusion

In this chapter, one of applications of hot electrons in laser cone plasma interactions – proton beam acceleration is studied. A new target design for a cone-shaped substrate, on the rear surface of which a proton layer is coated, is

proposed and demonstrated by 2D PIC simulations. It is shown that this scheme can increase the energy of protons and the coupling from laser to protons by about three times while maintaining the protons' monochromaticity. This effect is owed to the laser focusing and electron guiding by cone substrate.

The key for the generation of monoenergetic proton beams is the longitudinal size of proton layer which is coated on the rear surface of the heavy ion substrate. It is demonstrated that only ultrathin proton layer can experience the same electrostatic field and obtain monoenergy. From a simple estimate, 200 MeV monoenergetic proton beams may be achieved with the currently available PW laser facility.

Reference

1. Linlor, W.I., *Ion Energies Produced by Laser Giant Pulse.* Applied Physics Letters, 1963. **3**(11): p. 210-211.

2. Clark, E.L., et al., *Measurements of Energetic Proton Transport through Magnetized Plasma from Intense Laser Interactions with Solids.* Physical Review Letters, 2000. **84**(4): p. 670.

3. Maksimchuk, A., et al., *Forward Ion Acceleration in Thin Films Driven by a High-Intensity Laser.* Physical Review Letters, 2000. **84**(18): p. 4108.

4. Snavely, R.A., et al., *Intense High-Energy Proton Beams from Petawatt-Laser Irradiation of Solids.* Physical Review Letters, 2000. **85**(14): p. 2945.

5. Wilks, S.C., et al., *Energetic proton generation in ultra-intense laser--solid interactions.* Physics of Plasmas, 2001. **8**(2): p. 542-549.

6. Esirkepov, T.Z., et al., *Proposed Double-Layer Target for the Generation of High-Quality Laser-Accelerated Ion Beams.* Physical Review Letters, 2002. **89**(17): p. 175003.

7. Schwoerer, H., et al., *Laser-plasma acceleration of quasi-monoenergetic protons from microstructured targets.* Nature, 2006. **439**(7075): p. 445-448.

8. Kodama, R., et al., *Nuclear fusion: Fast heating scalable to laser fusion ignition.* Nature, 2002. **418**(6901): p. 933-934.

9. Sentoku, Y., et al., *Laser light and hot electron micro focusing using a conical target.* Physics of Plasmas, 2004. **11**(6): p. 3083-3087.

10. Nakamura, T., et al., *High Energy Electron Generation by Laser-Cone Interaction.* Plasma and Fusion Research, 2007. **2**: p. 018.

11. Flippo, K.A., et al., *Increased efficiency of short-pulse laser-generated proton beams from novel flat-top cone targets.* Physics of Plasmas, 2008. **15**(5): p. 056709-12.

12. Nakamura, T., et al., *Optimization of cone target geometry for fast ignition.* Physics of Plasmas, 2007. **14**(10): p. 103105-7.

Chapter 6 A New Method of Increasing Laser Intensity - Focusing of Intense Laser via Parabolic Plasma Concave Surface

6.1 Introduction

Laser intensity plays an important role for laser plasma acceleration, which is consistent with results in previous chapters. Equation (3.1) and (3.12) illustrate the amplitude of laser wakefield is proportional to the pump laser intensity. Temperatures of hot electrons from collisionless mechanisms also scale with laser intensity as $T_h \sim I^{1/2 - 1/3}$, and so does the energy of ions which is accelerated by the charge separation electrostatic field proportional to the temperature of hot electrons.

With the advent of chirped pulse amplification technique and the development of high-fluence laser materials, laser intensity can easily exceed 10^{18} W/cm^2. Higher laser intensity means higher electric and magnetic fields due to $E_0 = \sqrt{2I_0 / \varepsilon_0 c}$, where I_0 is the laser intensity, ε_0 is the permittivity of free space, c is the light speed in vaccum, and E_0 is the amplitude of electric field. In such high electric and magnetic fields, the motion of electrons is relativistic. Moreover, the index of refraction of optical media is strongly modified and the optics becomes highly nonlinear.

Laser intensity is $I_0=W/ST$, here W is the energy, T is the duration of laser, and S is the cross section of the laser beam. Higher input energy, shorter duration and smaller focal spot have advantages to obtain higher laser intensity. Under the current conditions of CPA technique, laser power is limited to hundreds of Terawatts to few of Petawatt. By focusing 17J pulse with width of 30fs onto a 0.8 μm focal spot through an f/1.0 parabolic mirror, researchers at the University of Michigan have achieved the highest recorded laser intensity of 2×10^{22} W/cm^2 [1]. However, it is difficult to obtain such a diffraction-limited focal spot because the geometric aberrations are highly sensitive to the alignment. The distortion of the wave envelope of laser beam by thermal effects and imperfection of optics also affects the focus. On the other hand, in real experiment of laser plasma interactions, such small f number parabolic mirrors can not be used to avoid plasma jet contaminating the mirror. So, in most CPA lasers for experiment around the world, the focal spots are from several to tens of microns.

In this chapter, an alternative scheme via parabolic plasma concave surface to focus intense laser is proposed. In the scheme, a parabolic concave surface is located at the focal spot of laser beam. The incident laser beam is then focused into a smaller

focal spot due to the geometric reflection. Due to the high reflection ratio of femtosecond laser, the focused laser intensity can be increased significantly. 3D PIC simulation is used to investigate the geometric focusing of parabolic plasma concave surface with different focal lengths, laser light polarizations.

Moreover, another concept of coherent harmonic focusing was presented by Gordienko [2]. It was demonstratedhigh harmonics with wavelength $\lambda_n=\lambda_0/n$ could be generated [3-5] in intense laser pulse overdense plasma interactions. Since the focal spot is proportional to the wavelength, high harmonics can be focused into smaller focal spot and higher intensity. Ref. [2] only discussed the this temporal focusing effect due to the generation of high harmonics. However, high harmonics also means the steepening and compression in time. Although the averaged laser intensities are the same for high harmonics and incident laser under the assumption of perfect reflection by a planar overdense plasma, the temporal laser intensity of high harmonics is much higher than that of the incident laser, and so are the temporal laser electric and magnetic fields. Such improvement of temporal laser fields can play an important role in the region of highly relativistic and nonlinear laser plasma interactions. In this chapter, this effect is demonstrated by the results of 3D PIC simulations.

6.2 PIC simulations

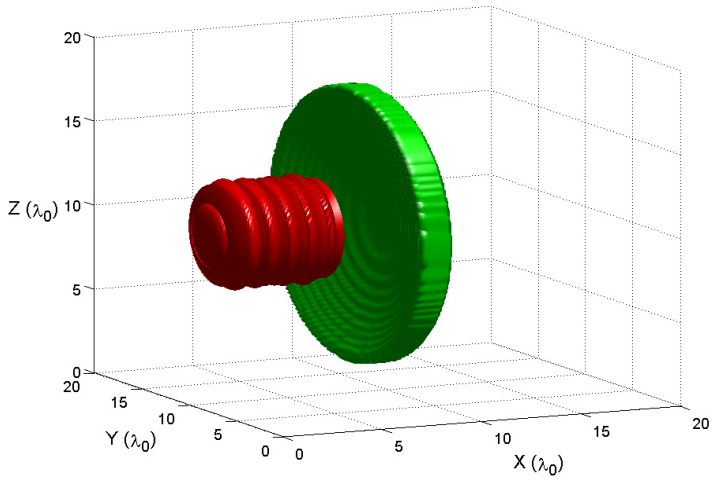

Figure 6.1 Scheme of focusing of intense laser via parabolic plasma concave surface

The parameters of 3D-PIC simulation are as follows. The longitudinal simulation length is $X = 20\lambda_0$, the transverse simulation length is $Y \times Z = 20\lambda_0 \times 20\lambda_0$. The cell

size is $\Delta X = \Delta Y = \Delta Z = 0.05\lambda_0$, so the number of spatial cells in the simulation system is $400\times400\times400$. The absorbing boundary for fields is applied in all directions. As for the particles, direct reflection boundary condition is applied in the transverse directions and thermal reflection boundary condition is employed in the longitudinal direction. The scheme of the focusing via parabolic plasma is shown in Figure 6.1. The plasma is homogeneous with density of five times critical density (n_e=5n_c). 27 simulation electrons and 27 simulation ions are placed in each cell. The surface of target is a parabolic plane with various focal lengths from 4μm to 16μm.

The Gaussian laser beam is irradiating the parabolic plasma from the left boundary. The focal spot w_0, for convenience here the waist of Gaussian beam is used instead of the FWHM, is $4\lambda_0$. The laser beam rises up in 2 laser cycles ($2\tau_0$) with a sinusoidal profile, after which it maintains its peak intensity for $6\tau_0$, and then falls down to zero in $2\tau_0$. The peak normalized vector potential at the w_0 is a_0=2.0, which corresponds to the incident intensity I_0=5.5×10^{18}W/cm^2.

If here optical reflection is assumed, the diffraction limit of the focal spot is $w=f\lambda_0/\pi w_0$, so the parabolic plasma with short focal length is of advantage for the focusing. But f should be larger than $w_0/2$ to make sure that the focal angle is smaller than 180°. So the minimum focal length employed in the present paper is $f= w_0$ and the corresponding diffraction limit of focal spot is λ_0/π. Due to the energy conservation $Iw^2 = \eta I_0 w_0^2$, where η is the reflectivity of the plasma, the limit laser intensity at the focus $I = \eta I_0 w_0^2 / w^2 = \eta I_0 \pi^2 w_0^4 / f^2 \lambda_0^2$. In the case of $f=w_0=4\lambda_0$ and η=1, the extreme intensity at focus can be up to 157.8I_0. In this simple way, the laser intensity can be increased more than two orders.

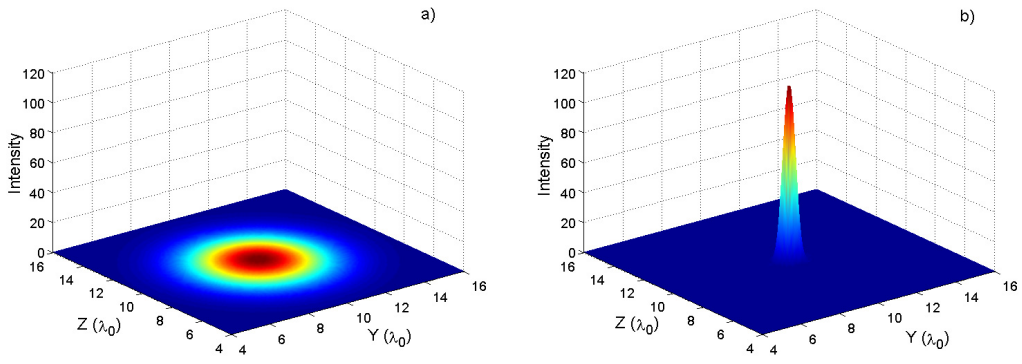

Figure 6.2 The radial profiles of a) the incident and b) the focused laser intensity, averaged over one laser period in YZ plane, from t=13τ_0 at X=2λ_0 for f=4λ_0.

Figure 6.2 demonstrates the focusing of intense laser by parabolic plasma via 3D PIC simulation. The radial profiles of the incident and the focused laser intensity, averaged over one laser period in YZ plane, from $t=13\tau_0$ at $X=2\lambda_0$ for $f=4\lambda_0$, are plotted in Figure 6.2 a) and b). 3D PIC simulation can show the focusing in the polarization plane and the transverse plane. From the data of Figure 2, for $f=4\lambda_0$, the waist of the focal spot is $0.53\lambda_0$, about 1.67 times of the diffraction limit. And the maximum focused intensity is $60.1I_0$, about 38.1% of the extreme intensity.

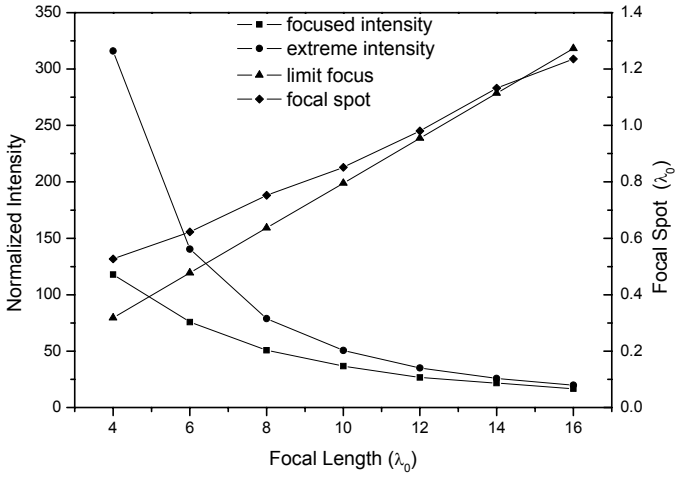

Figure 6.3 Extreme intensities (spherical), the focused intensities from PIC simulations (square), the limited focal spots (triangle) and the focal spots from PIC simulations (diamond) for various focal lengths.

Figure 6.3 shows the extreme intensities(spherical), the focused intensities from PIC simulations(square), the limited focal spots (triangle) and the focal spots from PIC simulations (diamond) for a variety of focal lengths. It is shown the focal spots are inversely proportional to the focal lengths of the parabolic plasma as expected. For small focal lengths, the differences between simulations and the extreme conditions are huge. However, when increasing the focal length, the focal spots of PIC simulation are getting closer to the diffraction limits, and so are the focused intensities. It can be interpreted by that the assumption of perfect optical reflection is not so correct, and density modulation of parabolic surface has strong effects on the laser reflection and focusing.

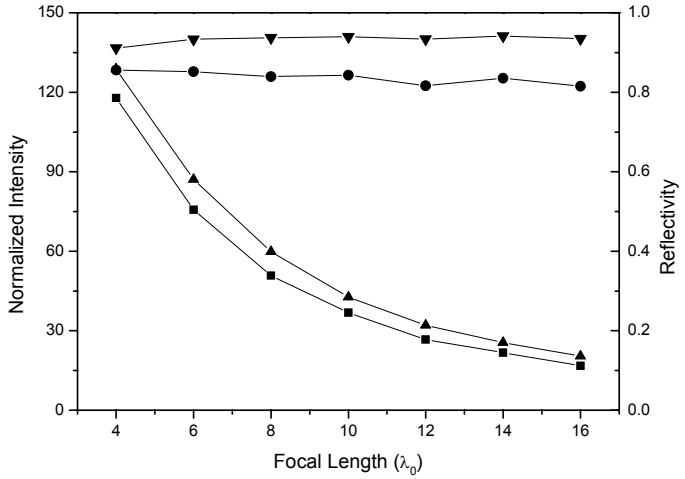

Figure 6.4 Reflectivity ratios for S-polarized laser light (down triangle), and P-polarized laser light (diamond); normalized focused intensities for S-polarized laser light (up triangle), and P-polarized laser light (square).

According to $I = \eta I_0 \pi^2 w_0^4 / f^2 \lambda_0^2$, the reflectivity also affects the focusing. Since linearly polarized laser has higher absorption than circularly polarized laser, the reflectivity of linearly polarized laser should be lower than circularly polarized laser. From the results of PIC simulations, there are no big differences of the focal spots for linear polarization and circular polarization. So the difference between the focused intensity is coming from the difference of reflectivity. It is elucidated in Figure 6.4 that the reflectivity of linear polarization is about 10% lower than that of circular polarization, and so is the corresponding focused intensity.

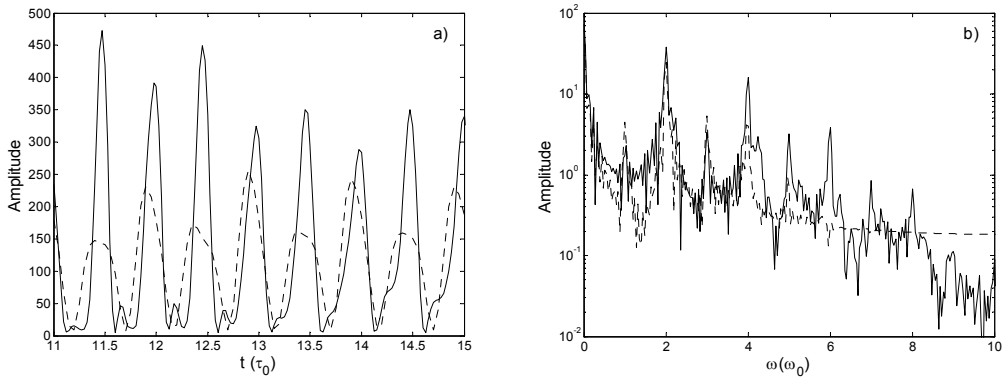

Figure 6.5 a) temporal distribution and b) spectrum of electric field in the case of Δx=0.05λ_0 (solid line) and Δx=0.1λ_0 (dashed line) along the laser axis.

Besides the geometric focusing of intense laser light by parabolic plasma concave surface, high harmonics generated in intense laser overdense plasma interactions can also contribute to the enhancement of laser intensity. The highest frequency which PIC programs can simulate is inversely proportional the cell size as $\omega_{max}=2\pi/\Delta t$, $k_{max}=2\pi/\Delta x$. To see the temporal compression of laser field, we use two kinds of cell size: one is $\Delta x=\Delta y=\Delta z= 0.1\lambda_0$ and the other is $\Delta x=\Delta y=\Delta z= 0.05\lambda_0$. Figure 6.5 a) shows the temporal distribution of focused laser electric field along the laser axis in the above two cases. For $\Delta x=0.1\lambda_0$ (dashed line), the maximum instant laser intensity is about $125I_0$. Meanwhile, for $\Delta x=0.05\lambda_0$ (solid line), the maximum instant laser intensity can reach as high as $230I_0$. The spectra of laser intensity for both cases are plotted in Figure 6.5 b). It is obviously shown that for finer cell size, the high harmonic components have higher amplitudes. It is these high harmonics that account for the temporal improvement of the focused laser.

6.3 Conclusion

Since laser intensity plays an important role determining the energy of accelerated particles, in this chapter, a new method of increasing laser intensity – focusing of intense laser via parabolic plasma concave surface is proposed. 3D PIC simulation is used to investigate the focusing of intense laser via parabolic plasma concave surface. The focusing includes two aspects: one is geometric focusing; the other is temporal and spatial high harmonics focusing. The results of PIC simulations demonstrate that these two effects both contribute to the improvement of laser intensity. It is expected the laser intensity especially the temporal laser intensity can be increased for several orders with parabolic plasma concave surface. Compared with the improvement of laser optics, this scheme is much more economic and appropriate for most of femtosecond laser facilities.

Reference

1. Yanovsky, V., et al., *Ultra-high intensity- 300-TW laser at 0.1 Hz repetition rate.* Opt. Express, 2008. **16**(3): p. 2109-2114.

2. Gordienko, S., et al., *Coherent Focusing of High Harmonics: A New Way Towards the Extreme Intensities.* Physical Review Letters, 2005. **94**(10): p. 103903-4.

3. Carman, R.L., D.W. Forslund, and J.M. Kindel, *Visible Harmonic Emission as a Way of Measuring Profile Steepening.* Physical Review Letters, 1981. **46**(1): p. 29.

4. Bulanov, S.V., N.M. Naumova, and F. Pegoraro, *Interaction of an ultrashort, relativistically strong laser pulse with an overdense plasma.* Physics of Plasmas, 1994. **1**(3): p. 745-757.

5. Gibbon, P., Harmonic Generation by Femtosecond Laser-Solid Interaction: A Coherent "Water-Window" Light Source? Physical Review Letters, 1996. **76**(1): p. 50.

Chapter 7 Summary

This thesis presented researches on laser plasma acceleration and relevant topics which are of significant importance to many exciting applications such as fast ignition inertial confinement fusion, laboratory astrophysics, medical cancer therapy, and so on. The new findings of this thesis are as follows

Chapter 3 Diagnostic of Nonlinear Laser Wakefield by Raman Scattering of Probe Laser Light

To help understand physics of laser wakefield acceleration for experiment, a diagnostic method measuring the amplitude of wakefield by Raman scattering of probe laser light is proposed in this chapter. An analytical solution and 1D simulation results for the multiple sidebands of the scattered probe laser pulse are presented. The convenience of this scheme is that the interval between the pump laser pulse and the probe laser pulse is not required to be controlled precisely in comparison with the other schemes, where the probe laser pulse width is shorter than the wakefield period and the probe pulse should be injected at a given phase of the wakefield. In the scheme of this chapter, since the probe laser pulse is longer than the wakefield wavelength, the accuracy of the injection timing could be a few wakefield wavelengths.

In the present scheme, the spectrum of the multiple sidebands can provide much detailed information about the wakefield by using the proposed analytical formula based upon 1D PIC simulations. The scheme of this paper is similar to the scheme that was discussed in a phenomenological way. The PIC simulations and the analytical results of this paper are consistent with the results of the experiment.

On the other hand, it is found that the wing structure in the scattered probe laser spectrum is useful for diagnosing the trapping and accelerating of electron bunches. Hence, it can be concluded that this diagnostic can be employed to measure laser wake field for a large parameter range of plasma density, plasma length and pump laser amplitude.

Chapter 4 Electron Acceleration in Laser-cone Interactions

Acceleration of hot electrons or the coupling from laser energy to electrons is the key issue of fast ignition of inertial confinement fusion and all other applications of

laser plasma interaction. Due to the guiding and focusing effect, cone target can increase the coupling efficiency significantly. This chapter studies acceleration of hot electron in intense laser cone plasma interactions via 2D PIC simulation.

The injection of hot electrons induced directly by the oblique incident laser on high gradient plasma surface is presented and investigated by theoretical analysis and 2D PIC simulations. It is demonstrated that high electric normal component can drag electrons into the vacuum to form the convex on the plasma surface. The convex affects the reflection of laser light so that the parallel component of electric field located at the foreside of the convex can pull it forward. This effect can generate high current along the plasma surface.

In the cone target scheme of fast ignition, 2D PIC simulation results show these energetic electron bunches are confined to the cone tip on the surface of cone wall and re-accelerated by the focused laser light at the cone tip. This re-acceleration effect has advantages of enhancement of energy of hot electrons and coupling from laser to hot electrons.

Moreover, it is shown that the energy flux through the cone tip using the double-layer cone target is much larger and more focusing than the single cone target. At the beginning of interaction, the sheath fields at the rear of inner cone wing are strong enough to confine the high energy electrons. But the sheath fields decrease to very low level after several hundreds of femtoseconds because of plasma expansion. In contrast, the quasistatic magnetic fields, which are generated by the surface current along the inner surface of the outer cone, can be still as high as 100MG even at a long time, which are the real reason for confining the high energy electrons.

Chapter 5 An Application of Hot Electrons by Laser Plasma Accelerator - Proton Acceleration in Laser cone Interactions

In this chapter, one of applications of hot electrons in laser cone plasma interactions – proton beam acceleration is studied. A new target design for a cone-shaped substrate, on the rear surface of which a proton layer is coated, is proposed and demonstrated by 2D PIC simulations. It is shown that this scheme can increase the energy of protons and the coupling from laser to protons by about three times while maintaining the protons' monochromaticity. This effect is owed to the laser focusing and electron guiding by cone substrate.

The key for the generation of monoenergetic proton beams is the longitudinal

size of proton layer which is coated on the rear surface of the heavy ion substrate. It is demonstrated that only ultrathin proton layer can experience the same electrostatic field and obtain monoenergy. From a simple estimate, 200 MeV monoenergetic proton beams may be achieved with the currently available PW laser facility.

Chapter 6 A New Method of Increasing Laser Intensity - Focusing of Intense Laser via Parabolic Plasma Concave Surface

Since laser intensity plays an important role determining the energy of accelerated particles, in this chapter, a new method of increasing laser intensity – focusing of intense laser via parabolic plasma concave surface is proposed. 3D PIC simulation is used to investigate the focusing conditions. The focusing includes two aspects: one is geometric focusing; the other is temporal and spatial high harmonics focusing. The results of PIC simulations demonstrate that these two effects both contribute to the improvement of laser intensity. It is expected the laser intensity especially the temporal laser intensity can be increased for several orders with parabolic plasma concave surface. Compared with the improvement of laser optics, this scheme is much more economic and appropriate for most of femtosecond laser facilities.

These research results majorly by PIC simulation method helped us understand the physics of laser plasma acceleration better, demonstrated the energy improvement of accelerated particles by target geometric design, estimated the possibility of generation of proton beams for the application of cancer therapy with currently available laser facilities, and offered a more economic method for increasing the laser intensity which is very important for producing high energy particles by laser plasma acceleration.

In conclusion, all of these researches contribute to the achievement of high energy particles and relevant applications from laser plasma acceleration.

Acknowledgments

I would like to express my gratitude to my supervisor, Prof. Kunioki Mima, for his enthusiastic support, motivation, and guidance throughout my work on this thesis. I am glad I had an honor of learning and working under the instruction of him.

I would as well like to thank all members of Computational and Theoretical Science on High Energy Density (CTH) group. Prof. Hideo Nagatomo supported me in every aspect of my studying in ILE. Dr. Tatsufumi Nakamura and Dr. Jun Zheng helped me a lot build the PIC programs for the simulation work. Dr. Takayoshi Sano, Dr. Atsushi Sunahara, Dr. Tomoyuki Jozaki, and Dr. Hongbo Cai all offered a great amount of valuable advices and discussions for my work.

I am grateful to Prof. Katsunobu Nishihara, Prof. Hiroshi Azechi, Prof. Kazuo Tanaka, Prof. Ryosuke Kodama, Prof. Hideaki Takabe, Prof. Hiroaki Nishimura, and Prof. Masakatsu Murakami for providing advanced laser plasma physics education which will be a treasure lasting all of my researching life.

I would as well like to thank Prof. Takahisa Jitsuno, Prof. Yoshio Ueda, and Prof. Toshiyuki Iida for the careful examination and creative suggestion for this thesis with their valuable time.

I also would like to thank all staffs of High Performance Computing and Networking (CMP) group who maintain the PC cluster system. Especially Mrs. Yuko Fukuda offered constructive suggestions for the performance and parallelization of my PIC codes on PC cluster.

I thank Ministry of Education, Culture, Sports, Science and Technology of Japan for the financial support by a Grant-in-Aid for Creative Scientific Research.

I thank Prof. Yongkun Ding, Prof. Hansheng Peng, Prof. Xiaoming Zhang, Prof. Yongjian Tang, Prof. Yuqiu Gu at Laser Fusion Research Center in Chinese Academy of Engineering Physics for their encouragement and support for my study and life.

I am deeply indebted to my dear family who have provided unquestioning support for the choices I have made in my life.

Major publications

Weimin Zhou, Kunioki Mima, Tatsufumi Nakamura, and Hideo Nagatomo, Probing of nonlinear evolution of laser wakefield by Raman scattering of laser light, Physics of Plasmas, **15**, 093107 (2008)

Weimin Zhou, Hongbo Cai, Hideo Nagatomo, Tomoyuki Johzarki, Atsushi Sunahara and Kunioki Mima, Proton Acceleration in the Interaction of Intense Laser with Cone Plasma Target and Coated Proton Layer, Plasma and Fusion Research, **3**, 062 (2008).

Weimin Zhou, Kunioki Mima, and Hideo Nagatomo, Particle-in-cell Simulation on the Measurement of Laser Wakefield with Raman Scattering of Probe Laser Light, Plasma and Fusion Research, **3**, 063 (2008).

Hong-bo Cai, Kunioki Mima, Wei-min Zhou, Tomoyuki Jozaki, Hideo Nagatomo, Atsushi Sunahara, and Rodney J. Mason, Enhancement of high energy electrons deposited to the compressed pellet via double cone in fast ignition, submitted to Physical Review Letter.

Other publications

Weimin Zhou, Yuqiu Gu, Xianlun Wen, and Chunye Jiao, Proton Jet from Interaction of TW Laser with Metal Foil Target on SILEX-I, Annual Progress Report 2005, Institute of Laser Engineering, Osaka University, 2005

Weimin Zhou, Kunioki Mima, Tatsufumi Nakamura, and Hideo Nagatomo, PIC simulation on cross-phase modulation of probe light by wakefield, Annual Progress Report 2007, Institute of Laser Engineering, Osaka University, 2007

Weimin Zhou, Hongbo Cai, Hideo Nagatomo, Tomoyuki Jozaki, Atsushi Sunahara and Kunioki Mima, Acceleration of Monoenergetic Protons in Ultraintense Laser-Cone Plasma Interactions, Annual Progress Report 2008, Institute of Laser Engineering, Osaka University, 2008

Presentations at academic conference

Weimin Zhou, One-dimensional PIC simulation on Stimulated Raman Scattering in intense laser-plasma interaction, the Physics Society of Japan, Kagoshima University, 2007

Weimin Zhou, Kunioki Mima, Phase modulation of probe light via laser induced wake field plasma wave, the Physics Society of Japan, Hogaido University, 2007

Weimin Zhou, Kunioki Mima, Tatsufumi Nakamura, Hideo Nagatomo,

Particle-in-cell simulation on proton acceleration using cone targets, the Physics Society of Japan, Kinki University, 2008

Weimin Zhou, Hongbo Cai, Kunioki Mima, Hideo Nagatomo, 3D PIC Simulation on the Focusing of Intense Laser via Parabolic Plasma, the Physics Society of Japan, Iwate University, 2008